Chromatin reprogramming and bone regeneration in vitro and in vivo via the microtopography-induced constriction of cell nuclei

Xinlong Wang[1,2,+], **Vasundhara Agrawal**[1,3,+], **Cody L. Dunton**[1,3], **Yugang Liu**[1,2], **Ranya K.A. Virk**[1,3], **Priyam A. Patel**[4], **Lucas Carter**[1,3], **Emily M. Pujadas**[1,3], **Yue Li**[1,3], **Surbhi Jain**[1,3], **Hao Wang**[5], **Na Ni**[5], **Hsiu-Ming Tsai**[6], **Nancy Rivera-Bolanos**[1,2], **Jane Frederick**[1,3], **Eric Roth**[7], **Reiner Bleher**[7], **Chongwen Duan**[1,2], **Panagiotis Ntziachristos**[8,9,10], **Tong Chuan He**[5], **Russell R. Reid**[11], **Bin Jiang**[1,2,8], **Hariharan Subramanian**[1,3], **Vadim Backman**[1,2,3,12,*], **Guillermo A. Ameer**[1,2,8,12,13,14,*]

[1]Department of Biomedical Engineering, Northwestern University, Evanston, IL 60208, USA

[2]Center for Advanced Regenerative Engineering, Northwestern University, Evanston, IL 60208, USA

[3]Center for Physical Genomics and Engineering, Northwestern University, Evanston, IL 60202, USA

[4]Quantitative Data Science Core, Center for Genetic Medicine, Feinberg School of Medicine, Northwestern University, Chicago, IL 60611, USA.

[5]Molecular Oncology Laboratory, Department of Orthopedic Surgery and Rehabilitation Medicine, The University of Chicago Medical Center, Chicago, IL 60637, USA

[6]Department of Radiology, The University of Chicago, Chicago, IL 60637, USA

[7]Department of Materials Sciences and Engineering, Northwestern University, Evanston, IL, 60208, USA.

[8]Department of Surgery, Feinberg School of Medicine, Northwestern University, Chicago, IL 60611, USA

[9]Department of Biochemistry and Molecular Genetics, Northwestern University, Chicago, IL, USA

[*]Correspondence and requests for materials should be addressed to V.B. (v-backman@northwestern.edu) or G.A.A. (g-ameer@northwestern.edu).
[+]These authors contributed equally to this work

Author Contributions Statement

X.W., V.A., V.B., and G.A. designed the experiments. X.W. and V.A. performed most experiments and analyzed the data. C.L.D. performed the imaging experiments on tissue samples and DN-KASH hMSCs. R.V helped with GSEA and transcriptional response analysis, P.P did the RNA-seq differential gene expression analysis, and J.F. assisted with the RNA-seq analysis. L.C performed the ATAC-Seq analysis. E.P performed the western blot and protein quantification analysis. Y.Li helped with the EM data collection and analysis. S.J. helped with transcriptional data interpretation and analysis. E.R and R.B. helped with ChromTEM sample preparation. X.W., Y.Liu., H.W., N.N., H.T., T.H., R.R., and G.A. designed and performed *in vivo* animal work. N.R. and C.D. helped with cell culture and sample preparation. X.W., V.A., B.J., P.N., H.S., V.B., and G.A. wrote the manuscript. All the authors discussed the results and reviewed the manuscript.

Competing Interests Statement

Code availability

Custom codes used in this study can be accessed on GitHub following this link (https://github.com/BME2021/LineageSpecificResponsiveness/blob/main/LineageSpecificResponsiveness.ipynb)

[10]Simpson Querrey Center for Epigenetics, Feinberg School of Medicine, Northwestern University, Chicago, IL, USA

[11]Laboratory of Craniofacial Biology and Development, Section of Plastic and Reconstructive Surgery, Department of Surgery, The University of Chicago Medical Center, Chicago, IL 60637, USA

[12]Robert H. Lurie Comprehensive Cancer Center, Northwestern University, Chicago, IL, USA

[13]Chemistry of Life Process Institute, Northwestern University, IL, 60208, USA

[14]International Institute for Nanotechnology, Northwestern University, Evanston, IL 60208, USA

Abstract

Topographical cues on cells can, through contact guidance, alter cellular plasticity and accelerate the regeneration of cultured tissue. Here we show how changes in the nuclear and cellular morphologies of human mesenchymal stromal cells induced by micropillar patterns via contact guidance influence the conformation of the cells' chromatin and their osteogenic differentiation *in vitro* and *in vivo*. The micropillars impacted nuclear architecture, lamin A/C multimerization and 3D chromatin conformation, and the ensuing transcriptional reprogramming enhanced the cells' responsiveness to osteogenic differentiation factors and decreased their plasticity and off-target differentiation. In mice with critical-size cranial defects, implants with micropillar patterns inducing nuclear constriction altered the cells' chromatin conformation and enhanced bone regeneration without the need for exogenous signalling molecules. Our findings suggest that devices with engineered surface topographies could be used to facilitate bone regeneration through engineering chromatin conformation states.

Introduction

Nuclear morphology is regulated by nuclear structure components such as lamins and chromatin, as well as cytoskeletal proteins.[1] Although not fully understood, studies have revealed that mammalian cells can modulate their nuclear morphology to adapt and acclimate to their microenvironments through the mechanotransduction process.[2–5] Usually, the nucleus is considered to be of spherical or ovoid shape, which is true for many types of cells. However, severe changes in nuclear morphology are also observed in various biological processes such as malignant cell invasion,[6] smooth muscle cell contraction,[7] stem cell homing,[8,] and embryo development.[9] As a cellular mechanosensor, changes in nuclear morphology are thought to directly affect chromatin architecture and genome functions that determine cell fate.[1] Contact guidance-induced nuclear deformation, similar to what occurs *in vivo*, can be reproduced *in vitro* using cells cultured on micro-and nano-pillar substrates.[10,11] The resultant nuclear deformation has been shown to affect phenotypic outcomes in stem cells such as proliferation and differentiation.[12–15] Although previous studies associate nuclear deformation on micropillars with MSC osteogenesis, direct evidence for contact guidance-induced chromatin reprogramming and targeted cell differentiation *in vitro* and *in vivo* is limited.[16] Furthermore, questions remain regarding the links between nuclear deformation and stem cell fate determination and whether such nuclear deformation can be a design parameter to improve the function of medical

devices *in vivo*. For instance, how nuclear deformation affects chromatin packing, and how the resulting alteration of chromatin packing regulates cell transcription, for example, to promote bone formation, remains elusive.

In this study, nuclear morphology changes were induced via contact guidance on micropillar patterns to investigate their influence on 3D chromatin conformation and transcriptional reprogramming in human mesenchymal stromal cells (hMSCs). Importantly, we demonstrate the biomedical significance of microtopography and chromatin engineering via contact guidance-induced nuclear deformation by documenting bone regeneration in a rodent cranial defect model. We hypothesized that mechanical constriction of the nucleus will lead to chromatin reprogramming, and as a consequence, modulate the transcriptional plasticity in stem cells to improve the efficiency of lineage-specific differentiation. Previously, we have demonstrated that the physical structure of chromatin packing regulates genome-wide transcriptional patterns by altering the kinetics of transcriptional reaction through macromolecular crowding-mediated effects exerted by chromatin density that is interrelated with the local chromatin nanoenvironment.[17] We uncovered that chromatin exhibits length-scale invariant scaling behavior within packing domains, with average sizes on the order of 200 kilo-base pairs (kbp) and 160 nm in diameter.[18] Specifically, we identified the packing density scaling of chromatin packing domains, *D*, as an important statistical descriptor of chromatin behavior and transcriptional plasticity. From a polymer physics definition, *D* defines the power-law scaling relationship between the genomic length of a polymer and the three-dimensional space it occupies. Furthermore, combining the molecular and physical regulators of transcription, the chromatin packing macromolecular crowding (CPMC) model predicts the effect of the average *D* on global patterns of gene transcription.[17] The model shows that an increase in *D* increases both the accessible surface area of chromatin, which determines the probability of genes being accessible to transcription factors and the heterogeneity of crowding conditions within a given transcriptional interaction volume. Therefore, given that *D* is one of the major predictors of global gene expression and phenotypic plasticity, we hypothesized that the differentiation outcomes in hMSCs can be modulated by potentially altering this physical property of chromatin. To address this hypothesis, we integrated microtopography engineering of biomaterials, nanoscale imaging, cell, and molecular biology to investigate the influence of severe nuclear deformation in hMSCs on chromatin conformation and transcription, as well as osteogenic differentiation (Fig. 1). In hMSCs, nuclear deformation caused changes in nucleoskeleton (lamin A/C) organization, and chromatin conformation, which is associated with increased transcriptional responsiveness to osteogenic differentiation cues, thus facilitating directed differentiation to the lineage. Implantation of hMSCs-seeded micropillar scaffolds promoted bone regeneration *in vivo*, without using exogenous signaling molecules, highlighting the advantages of microtopography engineering of biomedical implants and devices. Overall, we demonstrate contact guidance-induced nuclear deformation as a promising tool for chromatin engineering to facilitate transcriptional reprogramming in stem cells, allowing us to predictably control cell fate, especially to enhance the regenerative potential of stem cells.

Results

Micropillars alter nuclear morphology via cytoskeleton reorganization.

Micropillar structures were fabricated using methacrylated poly (octamethylene citrate) (mPOC) via contact printing (Supplementary Fig. S1A). A variety of parameters including pillar size, shape, and space were initially controlled to investigate their effects on nuclear morphology (Supplementary Fig. S1B–D). We found that micro-square pillars with size and spacing of 5×5 μm showed significant deformation in hMSC nuclei (Fig. 2A–C), characterized by a decrease in nuclear shape index (NSI) (Fig. 2D), nuclear volume (Fig. 2E), and surface area (Fig. 2F) based on the 3D reconstruction of the nuclei (Supplementary Fig. S1E). The projected area of the nuclei on micropillars was significantly smaller (Supplementary Fig. S1F), but the height was larger (Supplementary Fig. S1G). Additionally, the ratio of surface area to volume remains unchanged indicating a more compact shape of the nucleus (Supplementary Fig. S1H). The elastic modulus of the substrate is several hundred MPa (Supplementary Fig. S1I), which was shown to have no influence on cell morphology and nuclear deformation.[19]

In addition to nuclear morphology changes, cell morphology was also altered by surface topography. hMSCs cultured on a flat surface showed normal fibroblast-like spindle shape and formed well-organized cytoskeletal structures; whereas those cultured on micropillars showed elongated cell morphology with a weak assembly of the cytoskeleton (no actin cap and less cytoskeleton fibers) (Supplementary Fig. S2A). Cell adhesion, which is intimately related to the microenvironment and cytoskeleton assembly, was assessed by observation of vinculin at basal, central, and apical sides of cells on both flat and micropillar surfaces (Fig. 2G and Supplementary Fig. S2B–D). On a flat surface, hMSCs formed mature focal adhesions (FAs) only at the basal side. However, mature FAs were observed throughout the z-plane in hMSCs on micropillars indicating the micropillar topography can provide a more 3D microenvironment compared to a flat surface, which is defined as 2.5D culture. Although total expression of vinculin is similar on both surfaces (Supplementary Fig. S2E, F), more mature FAs were observed in cells on flat surfaces (Supplementary Fig. S2G), which contributed to a well-organized cytoskeleton assembly when compared to the micropillar surfaces (Supplementary Fig. S2B, C). These findings suggest the generation of higher cytoskeletal force in cells on a flat surface. Next, the influence of micropillars on mechanotransduction processes was investigated via YAP staining (Supplementary Fig. S2G). More nuclear YAP was observed in hMSCs cultured on flat surfaces (Supplementary Fig. S2H). Previous studies have shown that YAP-mediated mechanotransduction is influenced by cellular morphology.[20] To further investigate the influence of nuclear deformation on YAP activation, micropillars with size and spacing of 5×2 μm were fabricated to deform cell nuclei but limit cytoplasmic deformation to distinguish between the influence of cellular and nuclear deformation on nuclear accumulation of YAP. Nuclear deformation was maintained at the basal side but had similar FAs formation and F-actin assembly as those observed on flat surfaces (Supplementary Fig. S2I–K). Nuclear YAP remains on small-spacing micropillars, suggesting that cellular morphology disruption rather than nuclear deformation plays a critical role in YAP activation (Supplementary Fig. S2L, M).

Cytoskeletal components may concentrate external physical cues from the extracellular environment, making it possible for transferred local forces to trigger nuclear deformation.[21] To investigate the influence of the cytoskeleton on nuclear deformation, hMSCs were treated with 1 μM Latrunculin A, 4 mM acrylamide, and 1 μM colchicine to interfere with the assembly of F-actin, intermediate filaments, and microtubules, respectively. After 6 hours of treatment with latrunculin A and acrylamide, a significant increase in NSI was observed, while there was no significant change in NSI after treatment with colchicine indicating the involvement of F-actin and intermediate filaments in regulating nuclear morphology in hMSCs cultured on micropillars (Fig. 2H, I). Additional experiments were performed to investigate the influence of micropillars on hMSC function by quantifying cell attachment, metabolic activity, and proliferation (Supplementary Fig. S3). The results suggest that the micropillar structures attenuate hMSC proliferation and metabolic activity without affecting their viability.

Micropillars manipulate nuclear structure components.

The two key structural components of the nucleus- (1) nuclear lamina, which is primarily enriched in the nuclear periphery, and (2) chromatin, which has multiple tethering associations with the lamin at the nuclear periphery, contribute to the nuclear response to mechanical cues.[21–23] Recent studies reveal that cell culture substrates affect the polymerization of lamin A/C, which in turn influences the polarization of nuclear architecture and epigenetically regulates cell functions.[24–26] Additionally, chromatin organized into compacted domains that are enriched at the nuclear periphery may contribute to the response of the cell nucleus to forces.[27,28] We hypothesized that nuclear deformation in hMSCs induced by physical constriction is accompanied by alterations in nuclear structure components, including lamin A/C organization and chromatin-associated with the lamin at the nuclear periphery. To address this hypothesis, we firstly characterized lamin A/C organization on flat and micropillar surfaces. Horizontally, the lamin A/C was isotropically stained on flat surfaces (Fig. 3A and Supplementary Fig. S4A). However, it was anisotropically distributed in the cell nuclei on micropillars with high intensity of lamin A/C observed at nuclear protrusions and low intensity observed at the nuclear envelope (NE) in contact with micropillars (Fig. 3B and Supplementary Fig. S4B). In addition, distinct lamin A/C wrinkles were observed surrounding micropillars, which might be caused by the severe curvature of the cell nucleus in these regions. Vertically, the lamin A/C was anisotropically stained between the apical and basal NE in the cell nucleus on a flat surface but was isotropically distributed on micropillars (Fig. 3C and Supplementary Fig. S4C). The distinct distribution pattern of lamin A/C on flat surfaces and micropillars might be attributed to the different cell adhesion geometry and cytoskeleton assembly regulated via contact guidance (Fig. 3D).[24] Despite the different distribution patterns, the lamin A/C showed similar expression levels on both flat and micropillar substrates as tested by western blot (WB) analysis (Supplementary Fig. S4D, E).

Lamin-associated domains (LADs) are sensitive to alterations in lamin A/C at the nuclear periphery.[29] Also, changes in nuclear morphology, particularly nuclear volume can lead to variations in peripheral chromatin density profile.[29] Since the nuclear deformation resulted in a significant impact on the lamin A/C organization and nuclear volume, we hypothesized

that the organization of lamin-associated chromatin would be altered in micropillars. Using ChromTEM (Fig. 3E and Supplementary Fig. S5A), we evaluated chromatin mass density (Fig. 3F) to calculate the concentration of chromatin as a function of distance from the nuclear periphery within radial bands that refers to the 25 nm wide, consecutive, equidistant areas starting from the nuclear periphery and moving towards the nuclear interior (Fig. 3G). We found that the chromatin concentration is increased in hMSC nuclei on micropillar surfaces when compared to flat surfaces between 100 nm and 175 nm. This result suggests an increase in relocalization of heterochromatin-like domains, which are about 150 nm in diameter (Supplementary Fig. S5B–D) and are located towards the nuclear periphery in the deformed hMSC nuclei.

Nuclear deformation alters 3-D chromatin conformation in hMSCs.

Chromatin packing scaling (D) is a key physical property that is associated with transcription regulation and is also a crucial regulator of phenotypic plasticity.[17] To directly investigate the influence of nuclear deformation on chromatin reprogramming, we measured chromatin conformation from the level of packing domains in the mechanically constrained nucleus using partial-wave spectroscopic (PWS) microscopy that is capable of measuring D with sensitivity to length scales as small as 20 nm. Additionally, PWS enables the label-free sensing of nanoscale variations in supra-nucleosomal chromatin structure in both living and fixed cells.[30] Specifically, the variations in the chromatin packing density are measured using PWS in the form of a spectral interference signal originating from internal scattering within the cell nucleus. The shape of the autocorrelation function (ACF) of the chromatin density variations or the interference signal is then evaluated to determine the average nuclear D.[18,31] Relative to hMSCs cultured on a flat surface, hMSCs cultured on micropillars showed a decrease in whole-nuclear D of $8.01 \pm 0.74\%$ (SEM) in growth medium for 24 hours (Fig. 4A, B). Compared to the effect of other external cues, such as treatment with pharmacological agents for similar durations, such a change in D caused by topographical cues indicates a drastic change in chromatin conformation.[17,32] In addition, we investigated how micropillar-induced changes in D compared with those during osteogenic differentiation of hMSCs. We observed a significant decrease in D after day 1 of osteogenic induction. Such a decrease in D was also maintained in differentiating hMSCs on day 4 and day 14 of osteogenic induction (Supplementary Fig. S6). Average nuclear D of hMSCs was higher compared to osteo-induced progenitor and differentiated cells, consistent with our previous observations that higher D is associated with phenotypic plasticity.[17] Furthermore, by decreasing D, micropillars, may offer an efficient way to modulate this plasticity associated with hMSCs to enhance differentiation efficiency towards a target lineage.

To elucidate the effects of nuclear deformation on chromatin conformation below 20 nm, we employed ChromTEM to image chromatin in non-induced hMSCs on flat and micropillar surfaces. Since the nuclear deformation resulted in an increase in chromatin at the nuclear periphery, we hypothesized that the packing within lamina-associated, presumably heterochromatin-rich domains would be altered in micropillars. We evaluated the average ACF of chromatin mass density variations for both the whole nucleus and peripheral chromatin of hMSCs on micropillars compared to flat surfaces within 50–200

nm and 50–80 nm, respectively (Extended Data Fig. 1A). Next, to determine the D within these different regions, we fit a linear regression to the chromatin density ACF within the whole nucleus and the peripheral domains for each cell from both groups (hMSCs on flat and micropillars) on the log-log scale. We measured a $10.82 \pm 3.1\%$ (SEM) decrease in D for the whole nucleus in micropillars compared to a flat surface, which was comparable to the changes in nuclear D obtained using PWS. In addition, an $11.02 \pm 2.2\%$ (SEM) increase in D for peripheral chromatin in micropillars compared to a flat surface was obtained (Extended Data Fig. 1B). These findings suggest that mechanical constriction of the nucleus differentially alters the packing within chromatin domains located at the nucleus center and periphery. An increase in D in the peripheral chromatin and a decrease in average nuclear Dv may be a result of changes in phase separation of euchromatin and heterochromatin-like regions[33] and relocalization of dense chromatin domains towards the periphery (Fig. 3G).

We then used microtopography engineering to create hybrid micropillar patterns and delineate the influence of cellular (cytoskeleton) versus nuclear deformation on the nuclear organization. The hybrid micropillar patterns were designed to limit the degree of nuclear deformation while allowing cytoskeleton deformation similar to the typical 5×5 μm pillar design. We characterized the lamin A/C organization and chromatin structure in hMSCs cultured on these hybrid micropillar patterns. We found that using this hybrid micropillar pattern (Fig. 4C), the changes in cytoskeleton architecture are similar to those observed on the micropillar surface with 5×5 μm spacing (Supplementary Fig. S7A). However, the lamin A/C organization (Supplementary Fig. S7B–D) and D (Fig. 4D, E) do not change significantly in nuclei of hMSCs on hybrid micropillar patterns. This finding suggests that the non-uniform forces caused by the direct inhomogeneous contact of the nucleus with micropillar surfaces contribute to significant local strain on the nucleus. This increase in local nuclear tension due to the surface-induced constriction potentially leads to changes in lamin organization and chromatin conformation.

We also compared the average nuclear D of normal and DN-KASH transfected hMSCs (with the linker of nucleoskeleton and cytoskeleton (LINC) complex disruption) on flat and micropillar surfaces. We observed that D was decreased in DN-KASH hMSCs cultured on micropillar surfaces when compared to flat surfaces, which is similar to that observed in non-transfected (control) hMSCs (Extended Data Fig. 2). However, DN-KASH transduction did not significantly alter D. The experiments that used hybrid micropillar patterns (Fig. 4C–E and Supplementary S7) and DN-KASH hMSCs (Extended Data Fig. 2) confirmed that chromatin reorganization in deformed hMSCs was a consequence of direct mechanical constriction of the nucleus.[34] Therefore, cytoskeleton deformation alone is insufficient to cause a change in lamin A/C and chromatin organization in hMSCs cultured on micropillars.

Nuclear deformation increases the transcriptional responsiveness of hMSCs to osteogenic induction.

Changes in transcriptional plasticity of stem cells could enhance their ability to respond to a given induction cue, and in turn, increase their differentiation efficiency towards a specific lineage.[17] Therefore, we evaluated the lineage-specific responsiveness coefficient,

R_{LS}, defined as the average transcriptional response to an external differentiation stimulus of stem cells on a micropillar surface compared to a flat surface.

$$R_{LS} = \frac{\dfrac{E_{Induced,\,Pillar}}{E_{Stem,\,Pillar}}}{\dfrac{E_{Induced,\,Flat}}{E_{Stem,\,Flat}}}$$

(1)

Here E denotes the expression rate of a specific gene, and subscripts "induced", and "stem" refer to osteogenic differentiation induction and control conditions of stem cells, respectively. Using our bulk RNA-Seq data, genes were grouped based on initial pre-stimulated expression, and their change in average expression in response to an osteogenic differentiation stimulus was quantified in flat and micropillar populations (Fig. 4F). An increase in R_{LS} during hMSC differentiation in our case would indicate an increase in lineage-specific-transcriptional response on micropillars compared to a flat surface. In order to facilitate differentiation towards the targeted lineage on a given surface, the lineage-specific response should increase, $R_{LS} > 1$. Especially, at an early stage of differentiation, lineage-specific factors are initially lowly expressed in the stem cell state and therefore need to be stimulated further (upregulate or not downregulate as much in response to the induction cue).

Firstly, we employed our previously developed CPMC model, inputting our experimentally determined D for the micropillar versus flat surfaces, to predict the lineage responsiveness coefficient for genes that are upregulated and downregulated by differentiation induction. For initially lowly expressed genes in the stem cell state that are downregulated upon osteogenic induction, there is further downregulation in the higher D stem cells compared to the lower D stem cells on micropillars, which is shown by an increase in R_{LS} upon stimulation with osteogenic differentiation cues (Fig. 4G, orange curve). A similar trend was determined for the initially highly expressed genes, although the magnitude of the change was much smaller (Fig. 4G, purple curve). Altogether, the model predicted that, for lower D cells, genes with higher initial expression in stem cell conditions did not show as much downregulation or upregulation of genes associated with the stem state as the genes with initial lower expression. Next, we checked if such changes are also observed experimentally by analyzing our bulk RNA-seq data. A more drastic change in average expression in the hMSCs on micropillars compared to the flat surfaces was observed in the downregulated stem cell-associated genes in response to osteogenic differentiation stimulus. In agreement with our model predictions, we observed that the lineage-specific transcriptional response to osteogenic differentiation induction increased in low D cells on micropillars compared to high D cells cultured on flat surfaces, as R_{LS} was >1 for the majority of the set of genes grouped by initial control expression (Fig. 4G). Notably, genes with initially low expression in the control stem cell population exhibited a greater change in their global transcriptional profile on induction compared to initially highly expressed genes as predicted by the model.

To identify the transcriptional processes that guide changes in lineage-specific transcriptional responsiveness in hMSCs on micropillars, differential gene expression combined with gene ontology analysis was employed to determine the upregulated and downregulated processes in induced cells compared to control cells on flat surfaces. The processes identified in Supplementary Fig. S8A demonstrate a large cluster annotated to development-specific processes such as urogenital system development, blood vessel morphogenesis, epithelial cell differentiation, muscle structure development, etc., and a smaller cluster of bone development processes which included ossification, connective tissue, and skeletal system development. Additionally, we analyzed the effect of genes in these processes by evaluating the lineage-specific responsiveness coefficient, R_{LS}, for stem cells on micropillars compared to flat surfaces (Supplementary Fig. S8B). We notice that these development-specific genes follow a similar trend as previously observed, although less drastic than the identified differentially expressed genes in Fig. 4G. Altogether, these results indicate that micropillars increase the overall response of genes involved in lineage-specific processes with initial low expression in differentiating hMSCs, which may contribute to their increased osteogenic differentiation efficiency.

In addition to transcriptional responsiveness, we observed a change in nuclear YAP and cellular morphology in hMSCs upon osteogenic induction on micropillars. Compared to incubation in the growth medium, induced hMSCs on flat surfaces showed no obvious change in nuclear/cytoplasmic YAP and F-actin assembly on day 1 and day 7 of differentiation, respectively (Supplementary Fig. S9A, B). However, nuclear accumulation of YAP was observed on micropillars after 1-day osteogenic induction. hMSCs spread out and formed more stress fibers on micropillars after 7-day induction. These results confirm that mechanotransduction and cellular morphological responsiveness were also enhanced on micropillars.

To investigate the effects of nuclear deformation on the hMSC phenotype, we next evaluated the influence of micropillars on osteogenic differentiation of hMSCs upon induction. Three days post-induction, staining for RUNX2, which is one of the key transcription factors associated with osteogenic differentiation, showed stronger nuclear intensity and higher nuclear/cytoplasmic ratio in deformed nuclei indicating increased activation of RUNX2 on micropillars (Fig. 4H). Alkaline phosphatase (ALP) quantification demonstrated that micropillars promoted osteogenic differentiation of hMSCs after induction for 7 days (Fig. 4I). qPCR analyses of both early (ALP) and late (integrin-binding sialoprotein, IBSP) osteogenic related genes showed increased expression on micropillars (Fig. 4J). Additionally, calcium deposition in hMSCs was also enhanced on micropillars after 3 weeks of induction (Fig. 4K). Interestingly, the differentiated hMSCs further decreased NSI, which may be due to enhanced cytoskeletal tension after osteogenic differentiation (Supplementary Fig. S9C, D).[35] All these results demonstrate that nuclear deformation induced by micropillars promoted osteogenic differentiation of hMSCs *in vitro*.

Changes in gene expression due to micropillar-induced nuclear deformation are associated with alterations in chromatin accessibility.

To further confirm the influence of micropillar-induced nuclear deformation on gene expression and its relationship with chromatin state, we analyzed the transcriptional profile (RNA-Seq) and its overlap with the assay for transposase accessible chromatin by sequencing (ATAC-seq). The RNA-Seq principal component analysis (PCA) indicates that the micropillars make a significant impact on the hMSC transcriptome for both stem and induced cell states (Supplementary Fig. S10). From the RNA-Seq data (Fig. 5A), there is downregulation in processes associated with cell cycle and cell morphogenesis, while upregulation in processes associated with histone modifications in hMSCs cultured on micropillars (Fig. 5B). Additionally, in agreement with the CPMC modeling predictions, we also noticed upregulation in the expression of genes involved in response to external stimulus in hMSCs induced to differentiate towards the osteogenic lineage on micropillars (Fig. 5C). This finding indicates that micropillars may enhance the likelihood of osteogenic differentiation by enhancing the response of hMSCs to osteogenic medium. Next, to determine whether the processes identified using RNA-Seq are associated with a change in chromatin state or open chromatin regions, we investigated the processes associated with the intersection of the RNA-Seq and ATAC-Seq datasets. Using ATAC-Seq, we found that the top 1000 differentially identified regions indicate a more closed or repressed chromatin state in hMSCs cultured on micropillars (Fig. 5D). Interestingly, cellular processes associated with histone modifications, cell cycle, and growth are differentially expressed in the hMSCs cultured on micropillars (Table S1). Next, we evaluated the processes associated with both the differential open regions from the ATAC-Seq data and the differentially expressed genes from RNA-Seq data that are enriched and depleted in micropillars. Regions and genes associated with cell cycle, actin, focal adhesion, and response to DNA damage demonstrate a closed chromatin state and downregulation in hMSCs cultured on micropillar surfaces relative to controls (Fig. 5E). Additionally, regions and genes associated with processes such as a response to external stimulus and transcription factor binding demonstrate an open chromatin state and upregulation in hMSCs cultured on micropillar surfaces when compared to control (Fig. 5F).

Influence of micropillar-induced deformation on histone modifications.

Micro-engineered surfaces have been reported to modulate cell phenotype by influencing specific histone modifications.[36] As we observed transcription changes in genes associated with histone modification from RNA-Seq, we characterized the global epigenetic profile of hMSCs cultured on flat and micropillar surfaces in the growth medium using immunolabeling specific to several histone modifications (Extended Data Fig. 3A–C). We identified that expression of histone H3 acetylation (H3Ac) and tri-methylation of H3 at lysine 27 (H3K27me3), as well as nuclear expression of their upstream regulators including histone deacetylase 3 (HDAC3) and enhancer of zeste homolog 2 (EZH2), were significantly altered in the deformed nuclei compared to control (Extended Data Fig. 3D-G). Additionally, we studied the epigenetic fold change upon osteogenic induction as we had previously observed enhanced lineage-specific transcriptional responsiveness and change in cytoskeletal assembly on micropillars upon induction. Interestingly, the relative fold change of H3Ac, H3K27me3, HDAC3, and EZH2 were all enhanced on micropillars, indicating an

increased cellular response to osteogenic induction (Extended Data Fig. 4). To discriminate the influence of nuclear and cytoskeletal deformation on histone modification, we then tested the candidate epigenetic modifications, namely, H3Ac and H3K27me3 expression on the hybrid micropillar pattern (Extended Data Fig. 5). According to the results, both nuclear and cytoskeletal deformation significantly modulated histone modification levels in hMSCs cultured on micropillars.

Next, we investigated whether these repressive epigenetic modifiers, namely, EZH2 and HDAC3, that are enriched in the micropillars play a role in regulating chromatin conformation and phenotype in mechanically constricted hMSC nuclei. Using PWS microscopy, we find that upon inhibition of EZH2 and HDAC3, there was a small but significant effect on chromatin organization in hMSCs cultured on micropillars. The data suggest that these specific histone modification alterations also contribute to chromatin conformation on micropillars (Extended Data Fig. 6A). However, it should be noted that the magnitude of the influence of histone inhibitor treatment on chromatin conformation was much smaller than the change observed in the case of micropillars, indicating that mechanical constriction-induced nuclear deformation has a dominant role over candidate histone modifications on D. Additionally, the inhibition of EZH2 and HDAC3 did not significantly alter osteogenic differentiation of hMSCs on micropillars (Extended Data Fig. 6B, C), indicating that nuclear deformation-induced chromatin reprogramming was more dominant than alterations in histone modification in regulating gene expression related to fate determination in hMSCs.

Contact-guidance-induced nuclear deformation promotes bone recovery in calvarial defects in rodents.

Although our study and others demonstrate that hMSCs cultured on micropillars exhibit enhanced osteogenic differentiation *in vitro*,[13,14,37] the relevance of these findings to bone regeneration *in vivo* has not been evaluated to our knowledge. To further investigate the clinical relevance of using micropillar topography, especially in bone regeneration, hMSCs seeded flat and micropillar mPOC scaffolds were implanted in nude mice with critical-sized calvarial defects (Fig. 6A and Supplementary Fig. S11A). The calvarial defect model was chosen because skull bone is thin and amenable to the placement of 'films' that contain the topographies that will be investigated, and bone formation can be easily assessed. The cells seeded on free-standing mPOC micropillar scaffolds showed severe nuclear deformation, which was maintained after 1-week of implantation (Fig. 6B and Supplementary Fig. S11B, C). μCT scans were used to monitor defect size changes and new bone formation to evaluate the influence of micropillars on bone regeneration. According to the μCT results, treatment with micropillar implants accelerated healing around the defect edge at week 8 post-surgery (Fig. 6C, D and Supplementary Fig. S11E). In addition, newly formed bone can be observed within the defect region after 8 weeks of implantation of hMSCs seeded micropillar scaffolds. At 12-week post-surgery, the volume of newly formed bone in the defect region that was treated with micropillar implants was significantly higher than that treated with flat implants (Fig. 6E). The results are robust as we observed obvious new bone formation in 4 out of 5 animals implanted with micropillar scaffolds, but only 1 out of 5 animals implanted with flat scaffolds (Supplementary Fig. S11D).

Implant and tissue samples were collected at weeks 6 and 12 for histology analysis to further assess the effects of flat and micropillar implants on bone regeneration (Extended Data Fig. 7A). According to the H&E and trichrome staining images, more connective tissue and osteoid tissue formation were observed in defects treated with micropillar implants (Fig. 7A, B and Extended Data Fig. 7B, C). In addition, newly formed bone tissue was observed in defects treated with micropillar implants at 12-weeks. The thickness of newly formed tissue was significantly increased in the presence of micropillar implants (Extended Data Fig. 7F). Immunohistochemistry (IHC) staining of osteogenesis markers including osteopontin (OPN), osteocalcin (OCN), and Runt-related transcription factor 2 (RUNX2) showed a strong signal at the implant/tissue interface. (Fig. 7C and Extended Data Fig. 7D, E). Also, the tissues away from the interface were denser and showed stronger staining of osteogenic markers with the treatment of micropillar implants indicating enhanced osteogenesis. The micropillar structure also promoted better implant integration with surrounding tissue, which is critical for musculoskeletal tissue regeneration. Positive staining for anti-human nuclear antigen confirmed the presence and distribution of the hMSCs originally seeded on the implants. Human cells were not only located at the implant/tissue interface but also formed osteoid tissue together with mouse cells (Fig. 7D). Furthermore, PWS imaging of hMSCs within the tissue sections revealed a significant decrease in D for cells on micropillars confirming that contact guidance-induced nuclear deformation and chromatin conformation alteration persists *in vivo* (Fig. 7E).

Discussion

In the absence of external cues, the process of stem cell differentiation is typically stochastic in nature.[38] Biophysical chromatin reprogramming strategies via microtopography engineering may maximize directed differentiation to the cell type of interest. Specifically, this work demonstrates biophysical reprogramming of chromatin via contact guidance-induced nuclear constriction as a tool for chromatin engineering, to modulate cell plasticity and transcriptional responsiveness of stem cells to external differentiation cues. Herein, we demonstrate for the first time that microtopography engineering can be utilized to effectively modulate the stem cell phenotype, particularly, lineage-specific differentiation, via altering chromatin conformation and show that this approach can be used to accelerate bone regeneration *in vivo* using micropillar scaffolds fabricated from mPOC, a citrate-based biomaterial (CBB). CBBs have been shown to regenerate bone, are compatible with microfabrication techniques, are biodegradable, and elicit non-toxic anti-inflammatory responses.[39,40] CITRELOCK™, a biodegradable orthopedic fixation device fabricated from a CBB was recently cleared by the U.S. Food and Drug Admiration (FDA) (K200725.pdf (fda.gov)) and used clinically. Engineering the topography of orthopedic devices to include micropillars may result in enhanced bone apposition, improving device function and patient outcomes. Overall, our findings highlight how manipulating nuclear morphology using topographically engineered surfaces impacts chromatin conformation and gene transcription to control cell functions, which can in the future be used for various applications that extend beyond bone regeneration.

We utilized our toolbox of microtopography engineering and nanoscale imaging techniques to design hybrid micropillar patterns that allowed cytoskeleton deformation on micropillars

while limiting nuclear deformation. We showed that chromatin remodeling in hMSCs cultured on micropillars was modulated by changes in nuclear morphology due to micropillar-induced constriction. Chromatin reorganization in deformed nuclei was directly observed using PWS microscopy and ChromTEM. The results confirmed that compared to a flat surface, micropillars cause a significant decrease in D in the whole nuclei while an increase in local D at the nuclear periphery. Such drastic changes in the center and periphery of the nucleus in response to changes in nuclear morphology are indicative of the reorganization of chromatin compartments or transition between euchromatin-rich and heterochromatin-rich phases. Our previous study of structural and temporal changes of chromatin architecture using dual-PWS has shown that hMSCs have increased variations in both chromatin packing density and macromolecular motion within the nucleus than osteoblasts derived from them.[41] Based on the previously established CPMC model of transcription, D is directly related to transcriptional responsiveness. In accordance with CPMC model predictions, RNA-seq analysis combined with results from our microscopy experiments showed a decrease in average D in hMSCs nuclei using micropillars is accompanied by an increase in the stem cells' ability to respond to osteogenic differentiation induction at an early time point. Both our model predictions and experimental results demonstrate that differentiation on micropillars is more efficient than on flat surfaces, as micropillars can decrease chromatin packing in hMSCs, enhance the lineage-specific responsiveness and downregulate genes associated with the stem cell state. Therefore, contact guidance-induced chromatin reprogramming is a powerful tool that can be used to ultimately increase the differentiation efficiency of stem cells without the addition of exogenous bone-specific growth factors.

Additionally, we found that nuclear deformation via contact guidance-induced constriction played a more critical role in regulating chromatin structure when compared to LINC complex and certain histone modifiers. We make this conclusion because disruption of these components, which are key contributors in typical mechanotransduction processes, had limited effects on chromatin conformation. Other studies have suggested the involvement of cytoskeleton-driven mechanisms such as actomyosin contractility in regulating histone modification levels in the nuclei.[42,43] Furthermore, a recent study has highlighted the critical role of the LINC complex in regulating epigenetic/chromatin remodeling in deformed cardiomyocyte nuclei.[44] However, few studies have decoupled the effects of cytoskeletal and nuclear deformation on chromatin conformation. Our study utilizing microtopography engineering coupled with molecular inhibition studies highlights the direct effects of mechanical constriction on the nuclear architecture and altering D in hMSCs.

It is critical to determine the role of D in modulating stem cell phenotypes other than osteogenesis. Specifically, additional work investigating how nuclear reprogramming influences the movement of genes between and within domains or compartments in the 3D genome and transcription in constricted nuclei would be informative.[45] Studies involving chromatin conformation capture methods, gene labeling, combined with sequencing can be synergistically used to explore how a change in the spatial location of groups of genes, such as those associated with lineage/development can modulate their expression and eventually determine the cell fate or phenotype as a result of nuclear deformation. Additionally,

material microtopography should be considered for future design and fabrication of 3D scaffolds using advanced techniques (e.g. 3D printing) to further improve bone regeneration. For instance, features like the depth and spacing of the micropillars could be further optimized to modulate the efficiency of phenotypic outcomes at the tissue-implant interface.

To assess biomedical relevance, we implanted hMSC-seeded flat and micropillar scaffolds into critical-sized calvarial defects in mice to test the capacity of these surfaces to promote bone regeneration. The scaffold enhanced the retention of delivered cells and micropillar structures better promoted integration with surrounding tissue, which may be attributed to the increased surface area caused by the engineered topography. hMSCs migrated from the implant surface and formed connective and osteoid tissues together with the host cells. In addition, the implanted hMSCs may also promote bone formation through paracrine effects as transcription of various bone regeneration-related factors (e.g. VEGF, Wnt5A, TGF-β, etc.) were upregulated in deformed nuclei on micropillars (Table S2). Altogether, the micropillar implants facilitated bone formation and integration which are critical for bone regeneration. Application of microtopography engineering to other implants used in musculoskeletal surgery such as hip and knee implants, where maximum integration between implant and bone is desired to minimize aseptic loosening may result in better outcomes.

Materials and Methods

Synthesis and Characterization of mPOC Pre-polymer.

POC pre-polymer was firstly prepared according to the previous report.[46] Briefly, equal molar of citric acid and 1,8-octandiol were melted at 160 °C. Then, the mixture was transferred into a 140 °C oil bath and reacted for 30 min. The mixture was cooled down and dissolved in ethanol and purified by precipitation in DI water. The pre-polymer was lyophilized and used for the methacrylation process. 66 g POC pre-polymer was dissolved in 540 ml tetrahydrofuran (THF) and placed in a 60 °C water bath with stirring. Next, 0.036 mol imidazole was added into the system followed by drop-wise adding 0.4 mol glycidyl methacrylate. After reacting for 6 h, the solvent was removed using a rotary evaporator. The remaining product was purified by precipitation in DI water and lyophilized for further application. 5 mg mPOC pre-polymer was dissolved in 1 ml deuterated dimethyl sulfoxide (DMSO-d6) and characterized using proton nuclear magnetic resonance (^{1}H-NMR).

Fabrication of Micropillar Substrates.

The mPOC micropillars were fabricated using a combination of contact printing and UV lithography, and sterilized using ethylene oxide, and kept in DPBS before cell culture. Flat mPOC films were fabricated using the same method as flat PDMS molds. To fabricate substrates for ChromEM imaging, micropillars were directly fabricated on a cover glass using SU8-3010 which can reduce background and facilitate sample sectioning. The scaffolds for *in vivo* study were acquired by peeling of the flat and micropillar mPOC films from glass slides. A 4 mm diameter puncher was used to make the disk-like scaffold. After fabrication, the scaffolds were sterilized with UV light and rinsed with PBS, followed by incubation in complete medium for 24 h before cell seeding.

Cell Culture.

Human mesenchymal stromal cells (hMSCs, PCS-500-012) were purchased from the American Type Culture Collection (ATCC) and sub-cultured using a growth medium acquired from the same company. hMSCs (P4-P6) were seeded onto the flat mPOC substrates and the mPOC micropatterns with various microfeatures. To investigate the influence of micropillars on initial cell attachment, cells were seeded at 5000 cells/cm^2 onto flat and micropillar surfaces and incubated at 37°C, 5% CO$_2$ for 3h. After that, the substrates were rinsed with PBS twice and cells were dissociated with 0.05% trypsin-EDTA solution, followed by cell counting. Cell adhesion on mPOC substrates was evaluated by vinculin staining and western blot (Supplementary Fig. S12). Live/dead staining (Thermofisher, L3224) was performed after 3 days of culture to test cell viability. Cell metabolic activity was tested using an MTT assay (Thermofisher, V13154). Cell proliferation was tested by BrdU labeling and detection (Thermofisher, B23151) according to the manufacturer's protocol after 7 days of culture.

Cell Nuclear Deformation on Micropillars.

After one day of culture, the cells were fixed with 4% paraformaldehyde, and cell nuclei were stained with 4',6-diamidino-2-phenylindole (DAPI) to show nuclear morphology. The nuclear shape index (NSI) was calculated according to the staining images using the following equation: NSI $= 4\pi A/p^2$, in which A represents the area and p represents the perimeter. A total of 273 nuclei on flat surfaces and 295 nuclei on micropillar surfaces from 4 biological replicates were imaged and analyzed to calculate the statistics. In order to acquire 3D nuclear morphology, the stained cells were imaged using a confocal microscope (Leica SP8). The acquired images were analyzed using Fiji ImageJ software (https://imagej.net/Fiji) to measure cell nuclear volume, surface area, project area, height, and the ratio of surface area to volume (3D objects counter). A total of 33 nuclei on flat surfaces and 34 nuclei on micropillar surfaces from 3 biological replicates were imaged and analyzed to calculate the statistics.

Cytoskeleton Inhibition.

hMSCs were cultured on micropillars for one day before treatment of pharmacological agents. Specifically, F-actin filaments, microtubules, and intermediate filaments were disrupted with 1 μM Latrunculin A, 1μM colchicine; 4mM acrylamide, respectively. 6 h post-treatment, drugs were washed out and the cells were fixed and stained with Hoechst to show the nuclear morphology.

Immunostaining, Imaging, and Quantification.

Cells on flat and micropillar surfaces were fixed and permeabilized with 0.1% Triton-X100 followed by blocking with 1% BSA solution. Then, the primary antibodies (details in Supplementary Tables S3 and S4) were diluted in blocking solution and incubated with cells at 4°C overnight. After washing with a PBS buffer, secondary antibodies and Hoechst were diluted 1:1000 in PBS and incubated with cells at room temperature for 1h. The fluorescent images were acquired using a cytation 5 imaging reader and a Nikon eclipse TE2000-U inverted microscope with the software of NIS Elements AR. Histology images

were analyzed using ImageJ (1.50 i, NIH, Download (nih.gov)) according to a previous report.[47]

PWS Microscopy.

Bone Marrow-Derived Mesenchymal Stromal Cells (hMSCs) were cultured in 35 mm glass-bottom Petri dishes (Cellvis, Mountain View, CA) with a micropatterned or flat mPOC surface in growth medium or osteogenic differentiation medium at 37°C and 5% CO2. The PWS microscopy images were acquired on a commercial inverted microscope (Leica, Buffalo Grove, IL, DMIRB) with a Hamamatsu Image EM charge-coupled device camera (C9100-13) coupled to a liquid crystal tunable filter (CRi, Woburn, MA) to collect spectrally resolved images between 500 to 700 nm with 1 nm step size. Further, broadband illumination is provided by an Xcite-120 LED lamp (Excelitas, Waltham, MA). PWS microscopy was used to capture spatial variations of the refractive index distribution or chromatin packing density heterogeneity ($\sum$) within the nucleus. Further, the statistical parameter of chromatin structure, packing scaling (*D*) was calculated from $\sum$.[31] At least 10 independent fields of view were utilized for each experiment and four biological replicates were used for the analysis. *D* was calculated for 111 hMSCs from the flat surface, and 110 hMSCs on micropillar surfaces.

ChromTEM.

ChromTEM staining targets nuclear DNA specifically by utilizing the "click-EM" method.[48] Compared to conventional negative staining, which ubiquitously labels nucleic acid by uranyl acetate and lead citrate, ChromTEM provides us an opportunity to investigate chromatin organization from the perspective of DNA packing at high resolution. The image contrast for ChromTEM at the bright field for a thin resin section follows Beer's Law, which can be converted to DNA concentration with calibration:

$$I(x, y) = I_0 e^{-\sigma \rho(x, y)t}$$

(2)

Here $I(x, y)$ is the intensity of the resultant image, I_0 is the intensity of the incident beam, σ is the absorption coefficient of the sample, $\rho(x, y)$ is the density distribution, and *t* is the thickness of the section consisting of the sample. We assumed that for a given resolution, the absorption coefficient is constant. Further incident beam and section thickness was controlled to be the same across all images. Therefore, after taking a negative logarithm of the image followed by subtraction of the mean from the image, we directly obtain the chromatin density fluctuations from the image intensity.

The chromatin density obtained from the negative logarithm of the ChromTEM images of whole nuclei was utilized to evaluate the percentage of chromatin within 25 nm consecutive radial bands from the nuclear periphery to the center. This procedure was done to evaluate the radial distribution of chromatin from the nuclear envelope, as previously described.[49]

The chromatin density fluctuations can also be used to estimate ACF (autocorrelation function of chromatin density variations) using the Weiner Kinchen relation as previously described.[49] D can be evaluated using the power-law relationship of ACF approximated by:

$$ACF \sim r^{D-3}$$

(3)

where r is the spatial separation. This is followed by linear regression analysis to obtain the chromatin packing scaling for a given region within the nucleus. We were able to evaluate local chromatin packing D at different length scales within 50–200 nm by linear regressions on ACF on the log-log scale.

Differential Gene Expression and Gene Ontology analysis.

RNA extraction was performed on samples from flat and micropillar surfaces in both regular and osteogenic differentiation medium with at least two biological replicates per condition. Sequencing and library preparation were performed by Northwestern University NUSeq Core Facility. Illumina HiSeq 4000 Sequencer was used to sequence the libraries with the production of single-end, 50–base pair reads. The quality of reads, in fastq format, was evaluated using FastQC (http://www.bioinformatics.babraham.ac.uk/projects/fastqc). Adapters were trimmed, and reads of poor quality or aligning to rRNA sequences were filtered using Trim Galore (http://www.bioinformatics.babraham.ac.uk/projects/trim_galore/). The cleaned reads were aligned to the human genome (hg19) using STAR.[50] Read counts for each gene were calculated using HTSeq-Counts[51] in conjunction with a gene annotation file for hg19 obtained from Ensembl (http://useast.ensembl.org/index.html). A comprehensive QC report was generated using MultiQC. Differential expression was determined using DESeq2.[52] The cutoff for determining significantly differentially expressed genes was an FDR-adjusted p-value less than 0.05. The pathway analysis was done using Metascape.[53]

Osteogenic Differentiation of hMSCs.

hMSCs were seeded onto both flat and micropillar substrates. One-day post-seeding, an osteogenic induction medium (Lonza) was used to induce the osteogenic differentiation of hMSCs. After 7 d induction, the cells were washed with PBS buffer followed by fixation with 4% paraformaldehyde for 10 min. Immediately, the samples were merged in a solution of 56 mM 2-amino-2-methyl-1,3-propanediol (AMP, pH~9.9) containing 0.1% naphthol AS-MX phosphate and 0.1% fast blue RR salt to stain ALP. The bright-field images were then acquired using a Nikon Eclipse TE2000-U inverted microscope. The ALP activity was tested using the ALP assay kit (K422–500, Biovision) followed by the manual. Briefly, cells that have been cultured in an induction medium for 7 d were homogenized using ALP assay buffer. Then, the non-fluorescent substrate 4-Methylumelliferyl phosphate disodium salt (MUP) was mixed with the homogenized samples to generate a fluorescent signal due to its cleavage by ALP. The fluorescence intensity was read by a cytation 5 imaging reader (BioTek) at (Ex/Em = 360/440 nm). The enzymatic activity was calculated based on the standard curve and normalized to total DNA content tested by the Quant-iT

PicoGreen dsDNA assay (Invitrogen). Four biological replicates were used to calculate statistics. The expression of ALP and IBSP of hMSCs on flat and micropillar substrates was evaluated using quantitative real-time reverse transcription-polymerase chain reaction (RT-qPCR) after 7d induction. The total RNA of the cells was extracted using the Aurum Total RNA Mini Kit (bio-rad) according to the protocol. The concentration and purity of the extracted RNA were tested using the citation 5 imaging reader. The RT-qPCR was carried out using iTaq Universal Sybr Green One-step Kit following the vendor's protocol. The designed primers for ALP are: *Forward*, 5'-GACCCTTGACCCCCACAAT-3'; *Reverse*, 5'-GCTCGTACTGCATGTCCCCT-3'. The designed primers for IBSP are: *Forward*, 5'-TGCCTTGAGCCTGCTTCC-3'; *Reverse*, 5'-GCAAAATTAAAGCAGTCTTCATTTTG-3'. We employed GAPDH as the house-keeping gene. The GAPDH primers are: *Forward*, 5'-GTGGACCTGACCTGCCGTCT-3'; Reverse, 5'-GGAGGAGTGGGTGTCGCTGT-3'. The data was analyzed using the $2^{-\Delta\Delta Ct}$ method. The expression of target genes was firstly normalized to that of GAPDH, and then to the average values on flat substrates. Three biological replicates were used to calculate statistics. Calcium depositions were stained with Alizarin Red S on both surfaces after 3 weeks of induction. The positively stained area in the bright field images was analyzed using ImageJ software.

Lineage-specific Responsiveness Analysis.

Raw reads were aligned and mapped to the human hg38 ENSEMBL genome using bowtie2. Transcripts per million (TPM) for each condition were estimated from mapped reads using RSEM.[54] The lineage-specific responsiveness coefficient, R_{LS} was defined as the average transcriptional response to an osteogenic differentiation stimulus of cells on the micropillar surface compared to the flat surface. Genes with similar initial pre-stimulated expression, based on their quantile of $\log_2(E_{\mathrm{Induced}}/E_{\mathrm{control}})$, are grouped and their change in average expression in response to the stimulus is quantified in flat and micropillar populations for initially under-expressed and overexpressed genes. Further, GO analysis was done on DE genes with *p*-value<0.05 and |FC|>1.5 in induced cells compared to control cells to evaluate the lineage-specific responsiveness in biological processes that are involved in early differentiation.

ATAC-Seq Analysis.

(I) Read Trimming and Alignment: Adapter sequences were trimmed from Paired-end ATAC-seq FASTQ files using Trimmomatic[55] (version 0.39) to enable mapping fragments with sequences containing adapters using the following parameters and adapter sequences: ILLUMINACLIP:NexteraPE-PE.fa:2:30:10 LEADING:5 TRAILING:5 SLIDINGWINDOW:5:20 MINLEN:30. Trimmed reads were aligned to the most recent Human genome assembly, GRCh38.p13 (https://www.ncbi.nlm.nih.gov/assembly/ GCF_000001405.39) using Bowtie2 (version 2.4.1) with the parameters -X2000 and --very-sensitive. These parameters align fragments up to 2 kb and ensure a stringent alignment. Samtools[56] (version 1.10.1) was used to convert sequence alignment map (SAM) files to binary alignment map (BAM) files, sort these alignment files, and generate alignment statistics. For all alignments, duplicates were marked for later analysis, and alignment files were cleaned using PICARD tools (version 2.21.4) (http://picard.sourceforge.net).

(II) Filtering and Peak Calling: BAM alignments were introduced into R using Genomic Ranges[57] and Plyranges,[58] two popular packages for processing sequencing data, where alignment files were filtered to exclude nucleosome-bound fragments and fragments smaller than 20 base pairs. Reads were subsequently filtered for alignment quality of > Q30 and reads that were not properly paired were removed. Reads mapping to mitochondria and non-canonical chromosomes were removed at this stage of the analysis. Filtered BAM files were exported as BED files, where MACS2[59] (version 2.1.0) was used with the following parameters to call ATAC-seq peaks: -f BEDPE -g hs --nomodel --keep-dup all. For each condition, all ATAC peaks were merged in MACS2 as a single unity peaks file with a total of 215,998 peaks. *(III) Annotation, Differential Accessibility Analysis, and Enrichment Analysis:* Peaks were annotated by the promoter, intergenic regions, and exonic regions, and then labeled with the nearest genic region using ChIPseeker[60] annotation function. Using Genomic Ranges, we counted fragments for each sample across all peaks and generated a count matrix. This count matrix was subsequently filtered for near genic regions only, excluding distal intergenic regions, and peaks with low counts were filtered out. The reduced count matrix was then subset by the differential gene expression RNA-Seq results for a total of 79,078 peaks across all samples. Differential accessibility analysis to identify variable peaks between each contrast was then computed using DESeq2.[52] These results were analyzed for GO term enrichment using Cluster Profiler.[51] The differential accessibility results were then used to subset the differential gene expression results and analyzed for GO term enrichment using Metascape.[53]

Establishment of critical cranial defect model in nude mouse.

The animal study was approved by the University of Chicago Animal Care and Use Committee following NIH guidance (ACUP#71745). Eight-week-old female athymic nude mice obtained from Harlan Laboratories (Indianapolis, IN) were used for the study. The animals were housed in a separately air-conditioned cabinet at temperature of 24–26°C with 12:12 light:dark cycle. The surgeries were performed according to the previous report.[61] Briefly, animals were treated with 2% isoflurane delivered by 100% O_2 and maintained with 1%–1.5% isoflurane for anesthesia. Two critical sized defects (4mm diameter) were created on the left and right side of skull of each animal followed by implantation of hMSCs seeded flat and micropillar scaffolds, respectively. After implantation of scaffolds, a larger mPOC film (1×1.5 cm^2) was attached to the skull with thrombin/fibrinogen to prevent displacement of implants. Skin tissue was closed with 5–0 nylon interrupted sutures and removed after 2 weeks. The animals were monitored after anesthesia hourly until recovery. Buprenorphine 50 ug/kg and Meloxicam 1 mg/kg were used for pain relief.

Micro-CT imaging and analysis.

Micro-Computed Tomography (microCT) images of cranial were performed on the XCUBE (Molecubes NV., Gent, Belgium) by the Integrated Small Animal Imaging Research Resource (iSAIRR) at The University of Chicago. Spiral high-resolution CT acquisitions were performed with an x-ray source of 50 kVp and 440 μA. Volumetric CT images were reconstructed by applying the iterative image space reconstruction algorithm (ISRA) in a $400\times400\times370$ format with voxel dimensions of $100\times100\times100$ μm^3. An Amira software (Thermo Scientific) was used for 3D reconstruction of the skull tissue and to analyze the

bone formation in the defect area. Scale bars were used to standardize the images. Defect recovery is defined as $(V_i - V_d)/V_i \times 100\%$, where V_i and V_d represent defect volume at initial and designed time points, respectively.

Histological staining.

At 6 and 12 weeks post-surgery, the mice were euthanized with CO_2 inhalation and subsequent cervical dislocation. The skull samples were fixed and decalcified in Cal-EX II (Fisherscientific) for 24 h, followed by PBS rinsing and paraffin embedding. Then, the skull tissues containing defect sites were sectioned with 5 μm thick and subjected to H&E staining and trichrome staining to evaluate the tissue regeneration. The thickness of regenerated tissues was evaluated using ImageJ. Osteogenesis was evaluated by immunohistochemistry (IHC) staining of typical osteogenic markers including OCN, OPN, and RUNX2. Integration of hMSCs with host tissues was confirmed by staining of anti-human nuclear antigen. For all IHC staining, a negative control (without primary antibody incubation) and a negative tissue control (mouse skin tissue) were used for comparison.

Statistics and Reproducibility.

Most of the results are shown as mean ± S.D. using violin super plots.[62] Statistical analysis was performed using Kyplot software (version 2.0 beta 15). We also reported a standard error of the mean (SEM) with mean values in Fig 3G and 4G. Statistical significance was determined by the Student's t-test (flat vs. micropillar, two-sided) and one-way analysis of variance (ANOVA) with Tukey's post-hoc test (multiple groups). Chromatin packing scaling, *D*, was compared using the Bonferroni test among multiple groups. And a value of $p < 0.05$ was considered to indicate a statistically significant difference. For RNA-Seq analysis, the cutoff for determining significantly differentially expressed genes was a *p*-value less than 0.05 (*p*-value adjusted using the Benjamini–Hochberg procedure for multiple hypothesis testing). All experiments presented in the manuscript were repeated at least as two independent experiments with replicates to confirm the results are reproducible.

Extended Data
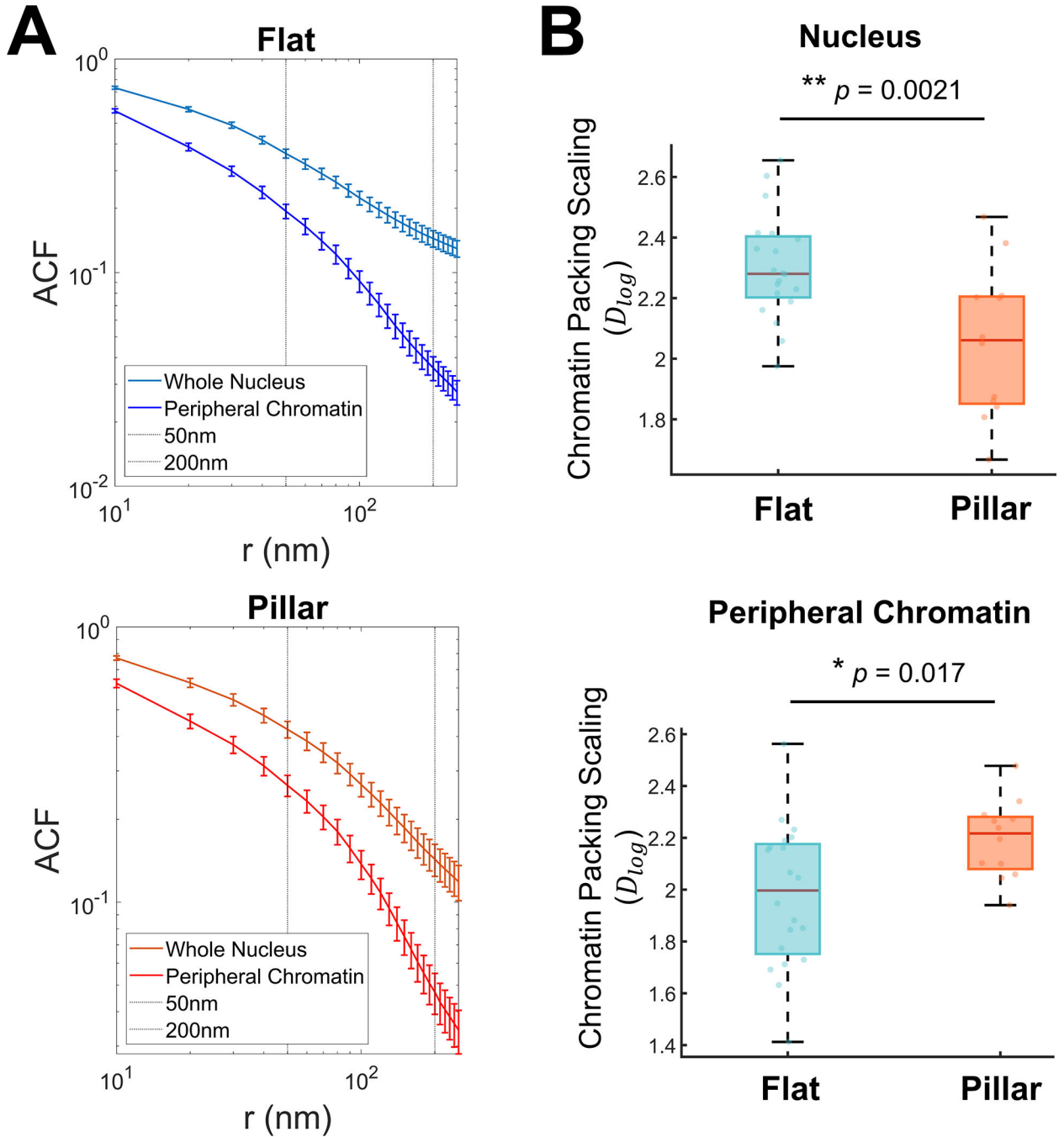
Extended Figure 1. ChromTEM validates a decrease in chromatin-packing scaling in deformed hMSC nuclei.

A. Spatial autocorrelation function (ACF) of chromatin density in the log-log scale for the whole nucleus, and peripheral chromatin. We obtained the chromatin-packing scaling by performing a linear regression of the ACF in the log-log scale within both 50–200 nm and 80–200 nm for the whole nucleus and within 50–80 nm for the nuclear periphery.
B. Chromatin-packing scaling shows a significant difference for whole-cell nuclei and

peripheral chromatin in hMSCs cultured on flat (n = 20 cells) and pillar surfaces (n = 12 cells), indicating a drastic change in the chromatin organization. N = 2 experiments. Statistics were compared using Student's t-test (two-sided). The lengths of the boxes indicate interquartile ranges (IQRs) of the first and third quartiles of samples, the horizontal lines represent the median values of the samples, and the whiskers indicate 1.5 IQR.
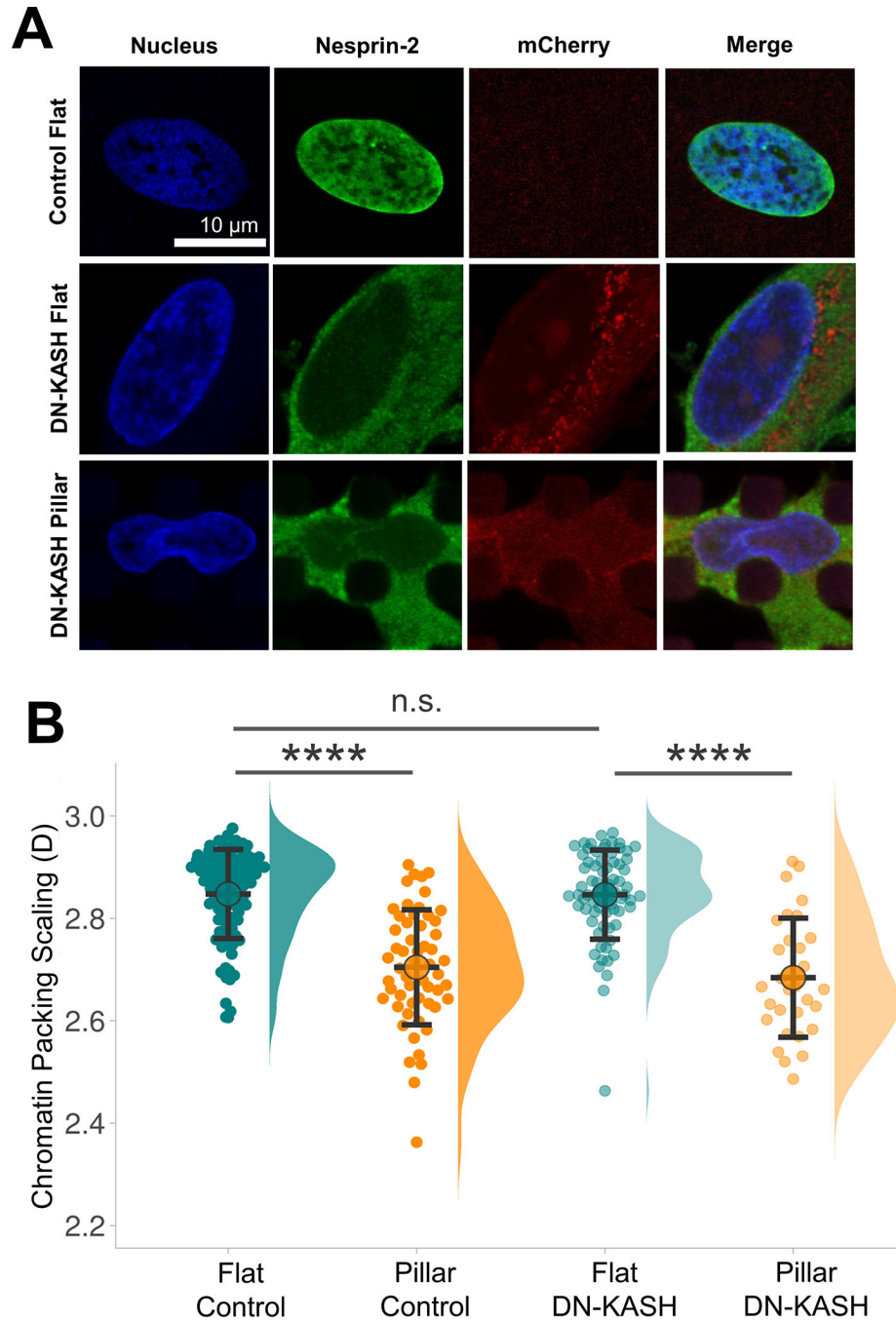
Extended Figure 2. Role of the LINC complex in regulating chromatin-packing scaling in hMSCs cultured on micropillars.

A. Representative images of Nesprin-2 and DAPI staining of mcherry tagged DN-KASH hMSCs cultured in flat and micropillar surfaces. Non-transfected cells on a flat surface were shown as a control. **B**. Disruption of the link between the nucleus and the cytoskeleton in DN-KASH hMSCs cultured on micropillars has limited effect on average D. hMSCs and DN-KASH hMSCs were cultured on flat (n = 95 cells, and 71 DN-KASH cells) and micropillar surfaces (n = 56 cells, and 30 DN-KASH cells). N = 3 experiments, ****p < 0.0001, n.s.=not significant. Data are presented as the mean and the standard deviation. Statistics were determined using Bonferroni's method for multiple comparisons.
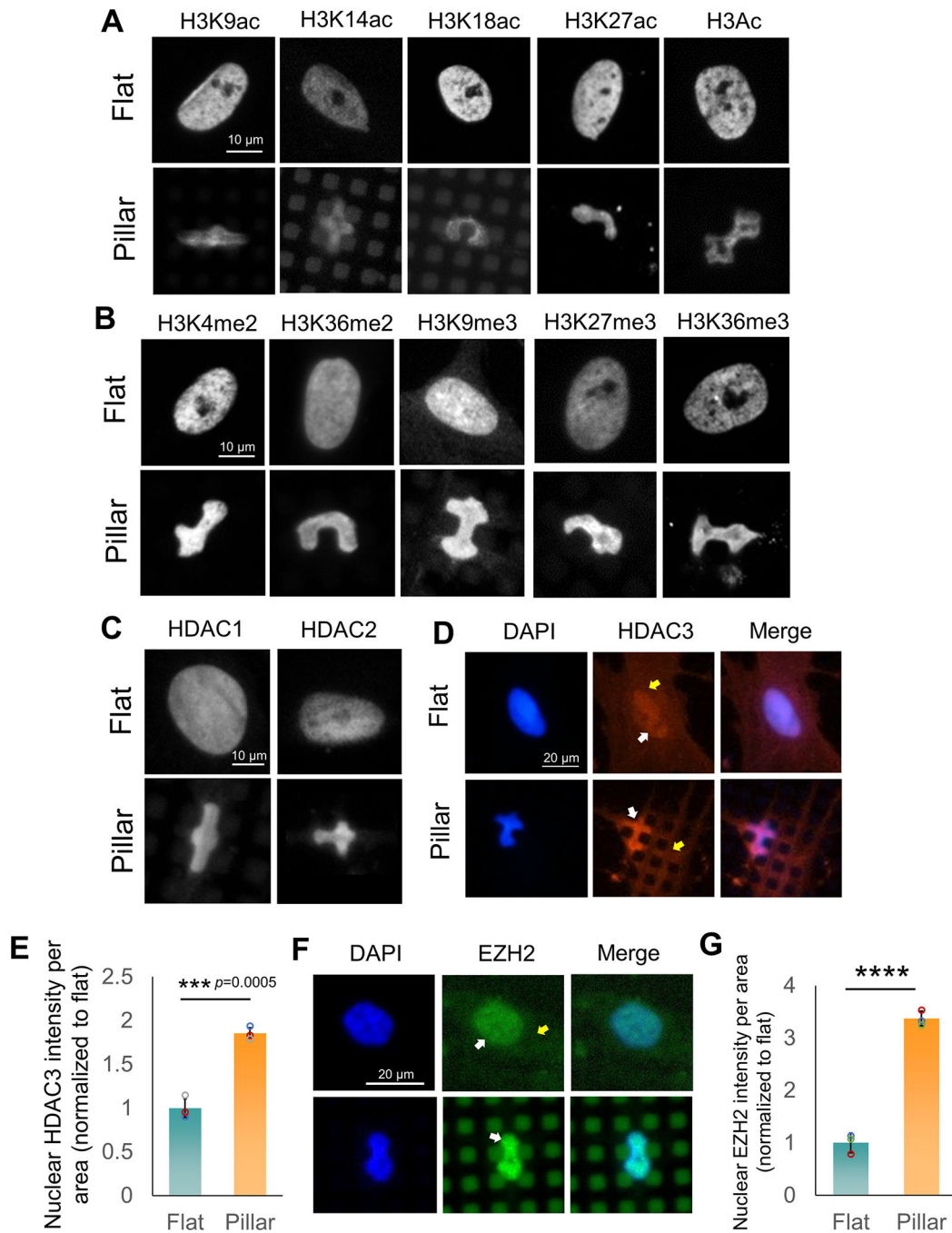
Extended Figure 3. Epigenetics profile of hMSCs cultured on micropillars in growth medium.
A. Immunostaining images of histone acetylation including acetylation of H3 at lysine 9 (H3K9ac), 14 (H3K14ac), 18 (H3K18ac), and 27 (H3K27ac), and total histone H3 acetylation (H3Ac) in hMSCs on flat and micropillar surfaces. **B**. Immunostaining images of active transcription markers include methylation of H3 at lysine 4 (H3K4me2) and 36 (H3K36me2 and H3K36me3), and repressive transcription markers include methylation of H3 at lysine 9 (H3K9me3) and 27 (H3K27me3) on flat and micropillar surfaces. **C**. Immunostaining images of histone deacetylase 1 (HDAC1) and 2 (HDAC2) in hMSCs

on flat and micropillar surfaces. **D**. Immunostaining images of HDAC 3 in cells on
flat and micropillar surfaces. White and yellow arrows indicate staining signals in the
nucleus and cytosol, respectively. **E**. Intensity ratio of nuclear HDAC3 to cytoplasmic
HDAC3 fluorescence intensity per area of cells on flat and micropillar surfaces. N = 3
experiments. **F**. Immunostaining images of EZH2 in cells on flat and micropillar surfaces.
White and yellow arrows indicate staining signals in the nucleus and cytosol, respectively.
G. Relative change of EZH2 expression compared to total H3 expression in cells. The
relative expression level on a flat surface was normalized to be 1 (****$p < 0.0001$, N =
3 experiments). Data are presented as the mean and the standard deviation. Statistics were
compared using Student's t-test (two-sided).
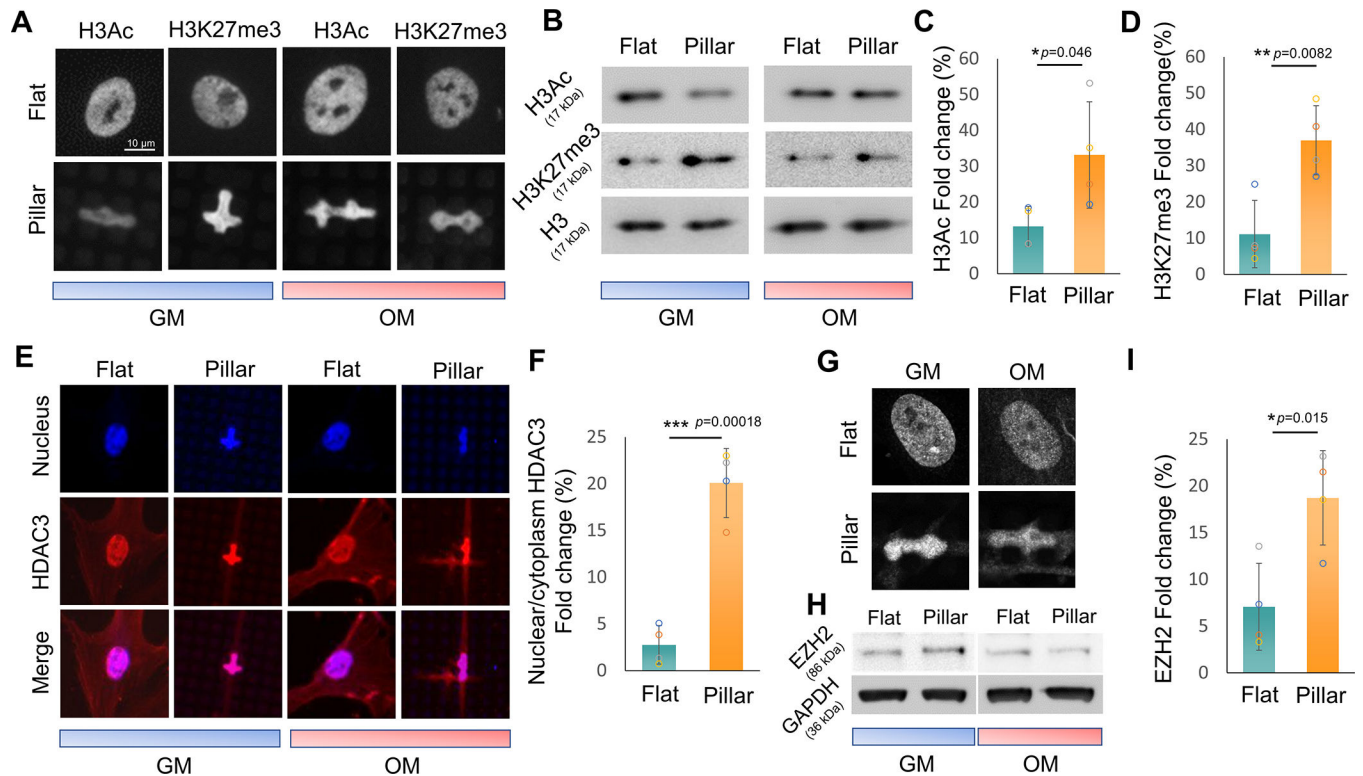
**Extended Figure 4. Characterization of enriched histone modifications on micropillar surfaces in response to osteogenic induction.**
A. Immunostaining images and **B**. western blot images of H3Ac and H3K27me3 in
cell nuclei on flat and micropillar surfaces cultured in GM (growth medium) and OM
(osteogenic induction medium). Total histone H3 is shown as a control. Osteogenic
differentiation induced fold change of **C**. H3Ac and **D**. H3K27me3 expression compared
to growth control on flat and pillar surfaces (n = 4 independent flat and pillar samples
cultured in GM and OM). The samples derive from the same experiment and that blots
were processed in parallel. **E**. Immunostaining images of HDAC3 in cell nuclei on flat
and micropillar surfaces cultured in GM and OM. **F**. Osteogenic differentiation induced
fold change that is intensity ratio of nuclear HDAC3 to cytoplasmic HDAC3 fluorescence
intensity per area of cells on flat and micropillar surfaces (n = 4 independent flat and pillar
samples cultured in GM and OM). **G**. Immunostaining images and **H**. western blot images

of EZH2 in cell nuclei on flat and micropillar surfaces cultured in GM and OM. GAPDH is shown as a control. **I**. Osteogenic differentiation induced fold change of EZH2 expression compared to growth control on flat and pillar surfaces (n = 4 independent flat and pillar samples cultured in GM and OM). The samples were derived from the same experiment and the blots were processed in parallel. Data are presented as the mean and the standard deviation. Statistics were compared using Student's t-test (two-sided).
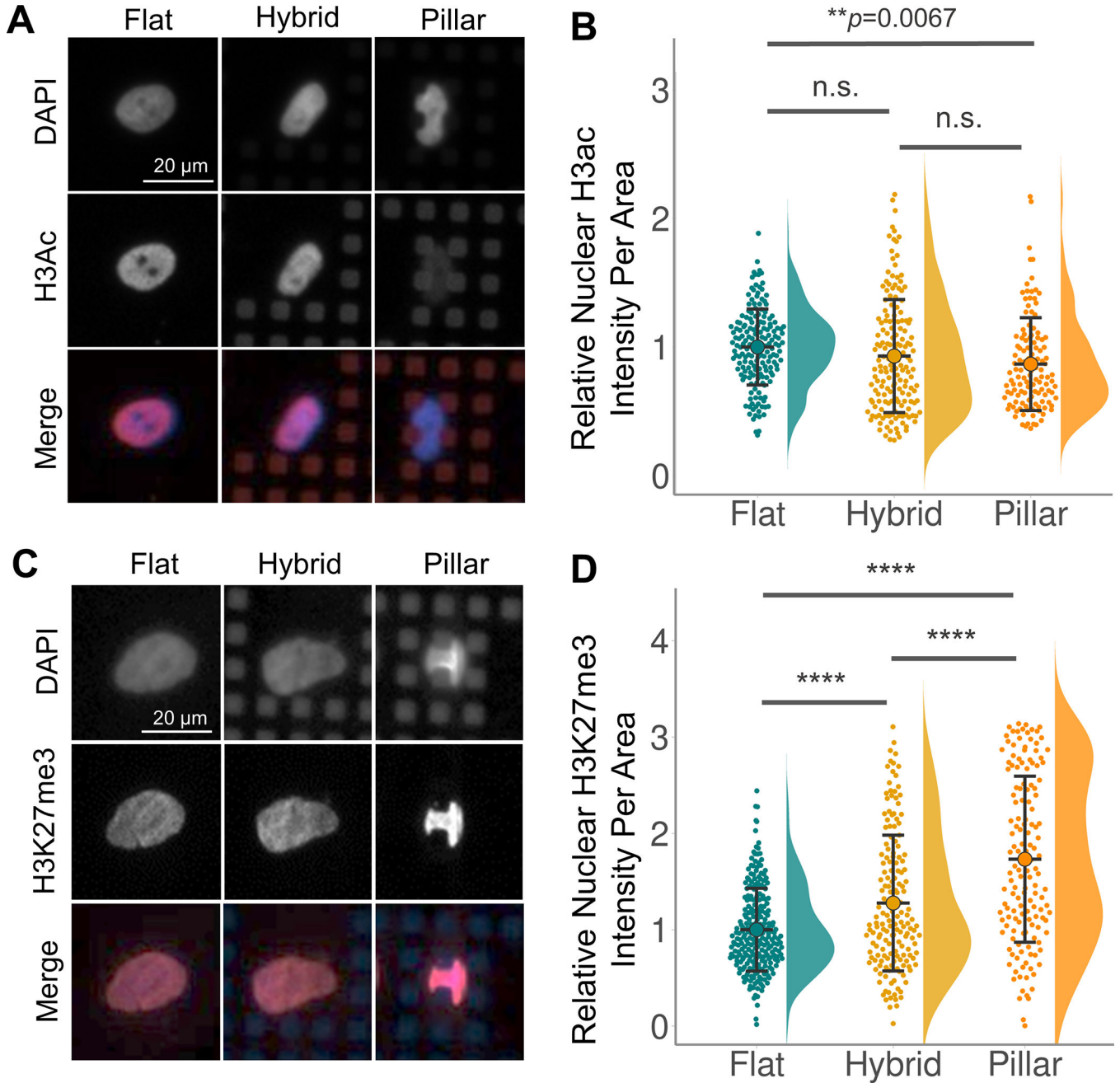
Extended Figure 5. Micropillar-induced cytoskeleton deformation modulates histone-modification levels.

Immunostaining images of **A**. H3Ac and **C**. H3K27me3 in cell nuclei on flat and hybrid micropillar surfaces cultured in growth medium. Nuclear/Cytoplasm intensity quantification of **B**. H3Ac and **D**. H3K27me3 expression in hybrid surface compared to growth control on flat and pillar surfaces (****$p < 0.0001$, n.s.= not significant, n = 175, 122, and 165 cells for H3Ac intensity analysis on flat, pillar and hybrid patterns; n = 245, 146, and 166 cells for H3K27me3 intensity analysis on flat, pillar and hybrid patterns over 3 independent experiments). Data are presented as the mean and the standard deviation. Statistics were compared using one-way analysis of variance (ANOVA) with Tukey's post-hoc test.
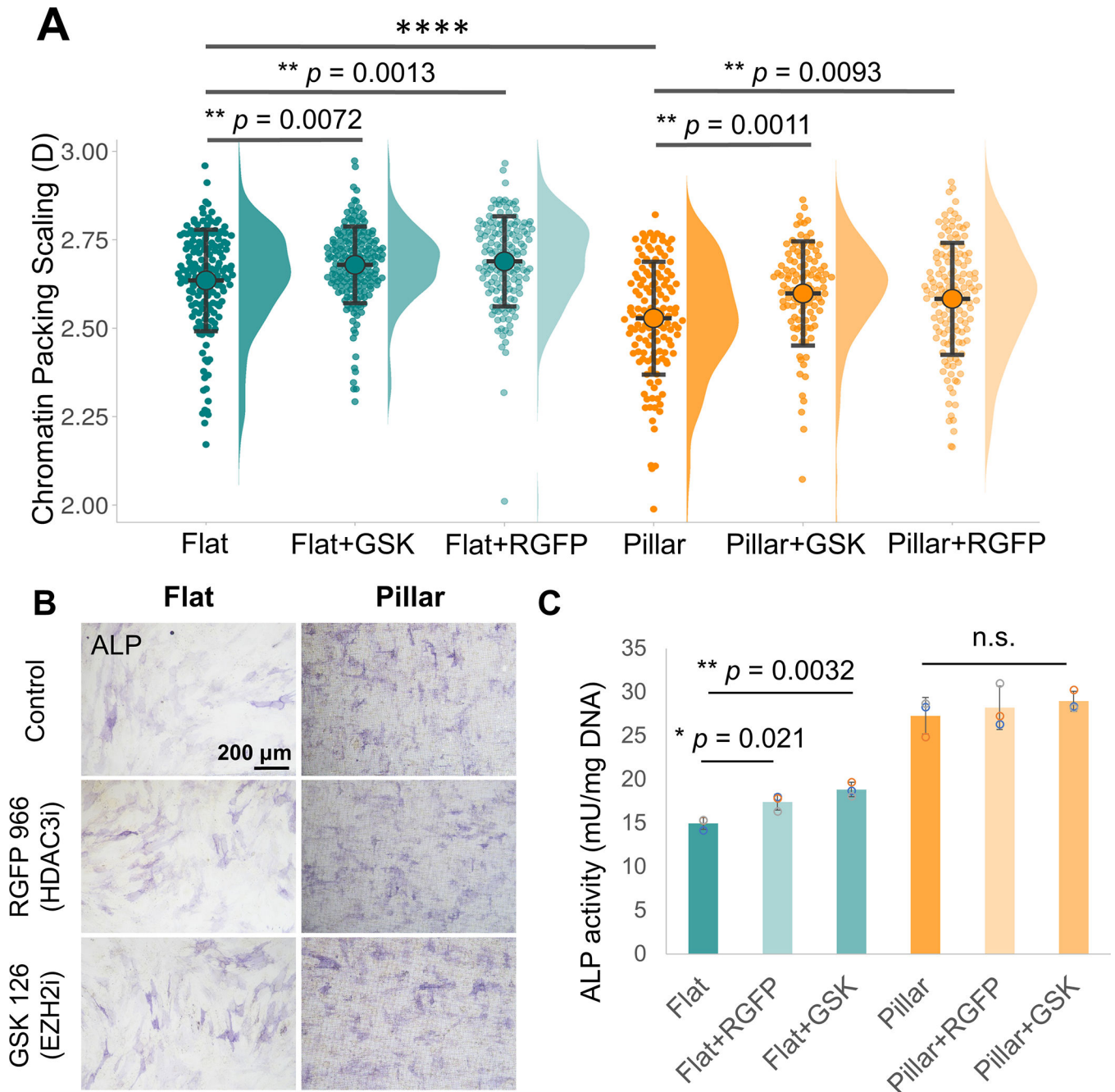
Extended Figure 6. Inhibition of candidate histone modifications in micropillars.
A. Chromatin conformation in hMSCs treated with GSK126 (EZH2 inhibitor) and RGFP966 (HDAC3 inhibitor) for 24 hours and seeded on flat and micropillar surfaces (n = 160, 186, 149, 135, 110 and 138 cells for flat, flat+GSK, flat+RGFP, pillar, pillar+GSK and pillar+RGFP groups, N = 3 experiments). **B**. ALP staining images. **C**. ALP activity analysis of hMSCs after 7-day osteogenic differentiation induction (****p < 0.0001, n.s.= not significant, n = 3 independent samples). Data are presented as the mean and the standard deviation. Statistics were compared using one-way analysis of variance (ANOVA) with Tukey's post-hoc test.
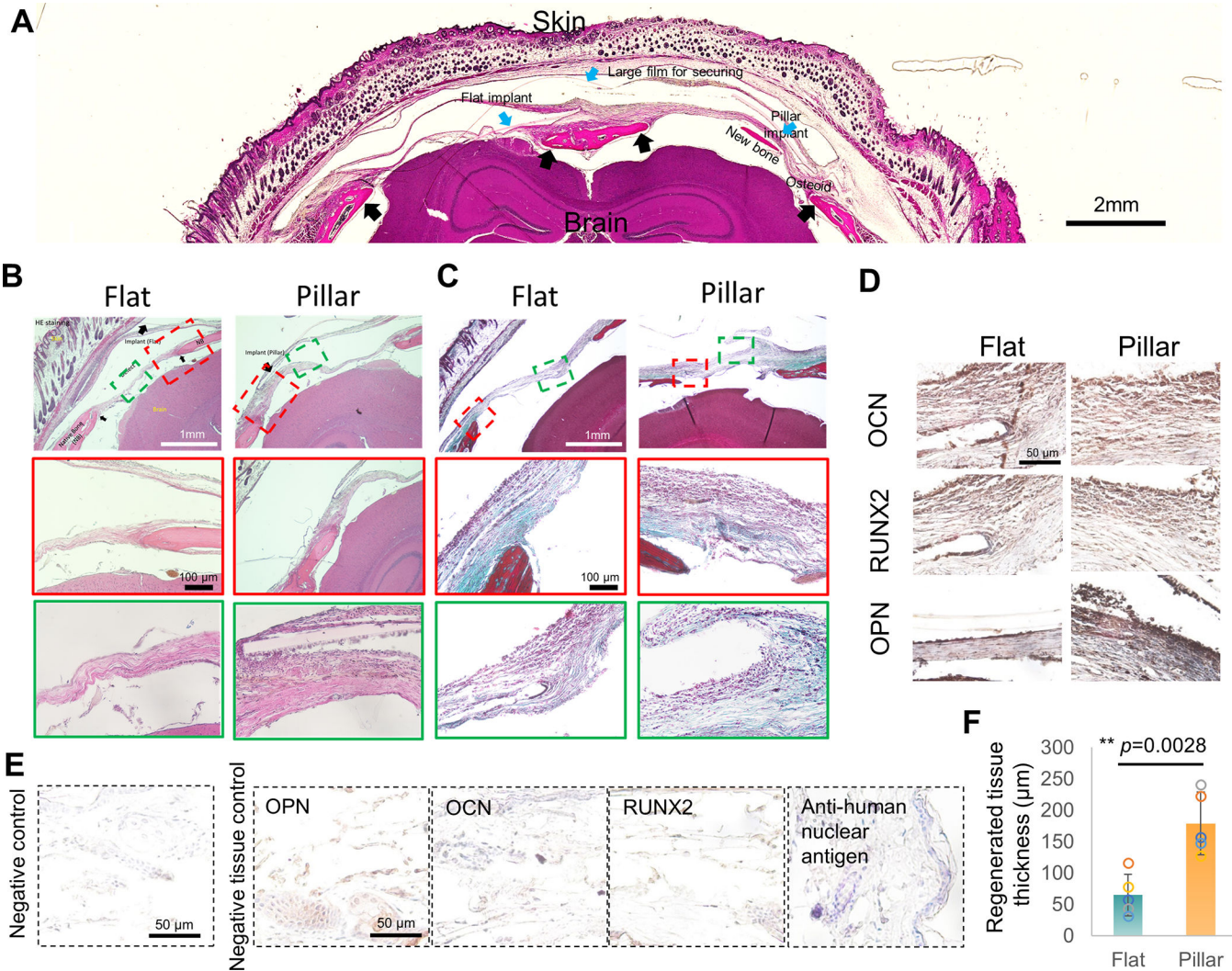
Extended Figure 7. Histological evaluation of flat and micropillar mPOC scaffolds induced cranial defect repair.
A. Gross images of mouse head showing the regenerated tissue with flat and micropillar implants. Black arrows indicate the edge of the defects. **B**. H&E and **C**. Masson's trichrome staining of cranial defects implanted with hMSCs seeded flat and micropillar scaffolds at 6-week post-implantation. Red and green frames indicate the tissue at the edge and central region of the wound. **D**. IHC staining of OCN, RUNX2, and OPN which are typical

osteogenesis markers at 6-week post-implantation. Stronger and thicker stained tissue was observed at the micropillar/tissue interface. **E.** Negative control (without primary antibody incubation) and negative tissue control (mouse skin tissue) of IHC staining. **F.** The thickness of regenerated tissue with flat and micropillar implants. n = 5 animals. Data are presented as the mean and the standard deviation. Statistics were compared using Student's t-test (two-sided).

Supplementary Material

Refer to Web version on PubMed Central for supplementary material.

Acknowledgments

Data availability

The main data supporting the results in this study are available within the paper and its Supplementary Information. The raw and analyzed datasets generated during the study are too large to be publicly shared, yet they are available from the corresponding authors upon reasonable request. All the sequencing data is available from the Gene Expression Omnibus (GEO) under accession code, GSE224265.

References

1. Dahl KN, Ribeiro AJS & Lammerding J Nuclear Shape, Mechanics, and Mechanotransduction. Cir. Res. 102, 1307–1318 (2008).

2. Alisafaei F, Jokhun DS, Shivashankar GV & Shenoy VB Regulation of nuclear architecture, mechanics, and nucleocytoplasmic shuttling of epigenetic factors by cell geometric constraints. Proc. Natl. Acad. Sci. U S A 116, 13200–13209 (2019). [PubMed: 31209017]

3. Swift J & Discher DE The nuclear lamina is mechano-responsive to ECM elasticity in mature tissue. J. Cell Sci. 127, 3005–3015 (2014). [PubMed: 24963133]

4. Uhler C & Shivashankar GV Nuclear Mechanopathology and Cancer Diagnosis. Trends in cancer 4, 320–331 (2018). [PubMed: 29606315]

5. Makhija E, Jokhun DS & Shivashankar GV Nuclear deformability and telomere dynamics are regulated by cell geometric constraints. Proc Natl Acad Sci U S A 113, E32–E40 (2016). [PubMed: 26699462]

6. Denais CM et al. Nuclear envelope rupture and repair during cancer cell migration. Science 352, 353–358 (2016). [PubMed: 27013428]

7. Roman W et al. Myofibril contraction and crosslinking drive nuclear movement to the periphery of skeletal muscle. Nat. Cell Biol. 19, 1189–1201 (2017). [PubMed: 28892082]

8. Lin C et al. Matrix promote mesenchymal stromal cell migration with improved deformation via nuclear stiffness decrease. Biomaterials 217, 119300 (2019). [PubMed: 31255981]

9. Pajerowski JD, Dahl KN, Zhong FL, Sammak PJ & Discher DE Physical plasticity of the nucleus in stem cell differentiation. Proc. Natl. Acad. Sci. U S A 104, 15619–15624 (2007). [PubMed: 17893336]

10. Davidson PM, Özçelik H, Hasirci V, Reiter G & Anselme K Microstructured Surfaces Cause Severe but Non-Detrimental Deformation of the Cell Nucleus. Adv. Mater. 21, 3586–3590 (2009).

11. Hanson L et al. Vertical nanopillars for in situ probing of nuclear mechanics in adherent cells. Nat. Nanotechnol. 10, 554–562 (2015). [PubMed: 25984833]

12. Pan Z et al. Control of cell nucleus shapes via micropillar patterns. Biomaterials 33, 1730–1735 (2012). [PubMed: 22133552]

13. Liu X et al. Subcellular cell geometry on micropillars regulates stem cell differentiation. Biomaterials 111, 27–39 (2016). [PubMed: 27716524]

14. Carthew J et al. Precision surface microtopography regulates cell fate via changes to actomyosin contractility and nuclear architecture. Adv. Sci. 8, 2003186 (2021).

15. Hasturk O, Ermis M, Demirci U, Hasirci N & Hasirci V Square prism micropillars on poly(methyl methacrylate) surfaces modulate the morphology and differentiation of human dental pulp mesenchymal stem cells. Colloids Surf. B 178, 44–55 (2019).

16. Stowers RS et al. Matrix stiffness induces a tumorigenic phenotype in mammary epithelium through changes in chromatin accessibility. Nat. Biomed. Eng. 3, 1009–1019 (2019). [PubMed: 31285581]

17. Virk RKA et al. Disordered chromatin packing regulates phenotypic plasticity. Sci. Adv. 6, eaax6232 (2020). [PubMed: 31934628]

18. Li Yue, et al. "Analysis of three-dimensional chromatin packing domains by chromatin scanning transmission electron microscopy (ChromSTEM)." Scientific reports 12, 12198 (2022). [PubMed: 35842472]

19. Badique F et al. Directing nuclear deformation on micropillared surfaces by substrate geometry and cytoskeleton organization. Biomaterials 34, 2991–3001 (2013). [PubMed: 23357373]

20. Dupont S et al. Role of YAP/TAZ in mechanotransduction. Nature 474, 179–183 (2011). [PubMed: 21654799]

21. Amar K, Wei F, Chen J & Wang N Effects of forces on chromatin. APL Bioeng. 5, 041503–041503 (2021). [PubMed: 34661040]

22. Briand N & Collas P Lamina-associated domains: peripheral matters and internal affairs. Genome Biol. 21, 85 (2020). [PubMed: 32241294]

23. Buchwalter A, Kaneshiro JM & Hetzer MW Coaching from the sidelines: the nuclear periphery in genome regulation. Nat. Rev. Genet. 20, 39–50 (2019). [PubMed: 30356165]

24. Ihalainen TO et al. Differential basal-to-apical accessibility of lamin A/C epitopes in the nuclear lamina regulated by changes in cytoskeletal tension. Nat. Mater. 14, 1252–1261 (2015). [PubMed: 26301768]

25. Kim D-H & Wirtz D Cytoskeletal tension induces the polarized architecture of the nucleus. Biomaterials 48, 161–172 (2015). [PubMed: 25701041]

26. Kim J-K et al. Nuclear lamin A/C harnesses the perinuclear apical actin cables to protect nuclear morphology. Nat. Commun. 8, 2123 (2017). [PubMed: 29242553]

27. Kalverda B, Röling MD & Fornerod M Chromatin organization in relation to the nuclear periphery. FEBS Lett. 582, 2017–2022 (2008). [PubMed: 18435921]

28. Maeshima K, Tamura S & Shimamoto Y Chromatin as a nuclear spring. Biophys. Physicobiol. 15, 189–195 (2018). [PubMed: 30349803]

29. Amiad-Pavlov D et al. Live imaging of chromatin distribution reveals novel principles of nuclear architecture and chromatin compartmentalization. Sci. Adv. 7 (2021).

30. Almassalha LM et al. Label-free imaging of the native, living cellular nanoarchitecture using partial-wave spectroscopic microscopy. Proc Natl Acad Sci U S A 113, E6372–e6381, doi:10.1073/pnas.1608198113 (2016). [PubMed: 27702891]

31. Eid A et al. Characterizing chromatin packing scaling in whole nuclei using interferometric microscopy. Opt. Lett. 45, 4810–4813 (2020). [PubMed: 32870863]

32. Almassalha LM et al. Macrogenomic engineering via modulation of the scaling of chromatin packing density. Nat. Biomed. Eng. 1, 902–913 (2017). [PubMed: 29450107]

33. Bajpai G, Amiad Pavlov D, Lorber D, Volk T & Safran S Mesoscale phase separation of chromatin in the nucleus. eLife 10 (2021).

34. Killaars AR, Walker CJ & Anseth KS Nuclear mechanosensing controls MSC osteogenic potential through HDAC epigenetic remodeling. Proc. Natl. Acad. Sci. U S A 117, 21258–21266 (2020). [PubMed: 32817542]

35. Yourek G, Hussain MA & Mao JJ Cytoskeletal changes of mesenchymal stem cells during differentiation. ASAIO J. 53, 219–228 (2007). [PubMed: 17413564]

36. Downing TL et al. Biophysical regulation of epigenetic state and cell reprogramming. Nat. Mater. 12, 1154–1162 (2013). [PubMed: 24141451]

37. Hasturk O, Ermis M, Demirci U, Hasirci N & Hasirci V Square prism micropillars improve osteogenicity of poly(methyl methacrylate) surfaces. J. Mater. Sci. Mater. Med. 29, 53 (2018). [PubMed: 29721618]

38. Gjorevski N et al. Tissue geometry drives deterministic organoid patterning. Science 375, eaaw9021 (2022). [PubMed: 34990240]

39. Wang Y, Kibbe MR & Ameer GA Photo-crosslinked biodegradable elastomers for controlled nitric oxide delivery. Biomater. Sci. 1, 625–632 (2013). [PubMed: 24707352]

40. Ware HOT et al. High-speed on-demand 3D printed bioresorbable vascular scaffolds. Mater. Today Chem. 7, 25–34 (2018).

41. Gladstein S et al. Multimodal interference-based imaging of nanoscale structure and macromolecular motion uncovers UV induced cellular paroxysm. Nat. Commun. 10, 1652 (2019). [PubMed: 30971691]

42. Heo S-J et al. Chemo-Mechanical Cues Modulate Nano-Scale Chromatin Organization in Healthy and Diseased Connective Tissue Cells. BioRxiv, 441596, doi:10.1101/2021.04.27.441596 (2021).

43. Damodaran K et al. Compressive force induces reversible chromatin condensation and cell geometry–dependent transcriptional response. Mol. Biol. Cell 29, 3039–3051 (2018). [PubMed: 30256731]

44. Seelbinder B et al. Nuclear deformation guides chromatin reorganization in cardiac development and disease. Nat. Biomed. Eng. 5, 1500–1516 (2021). [PubMed: 34857921]

45. Uhler C & Shivashankar GV Regulation of genome organization and gene expression by nuclear mechanotransduction. Nat. Rev. Mol. Cell Biol. 18, 717–727 (2017). [PubMed: 29044247]

46. van Lith R, Wang X & Ameer G Biodegradable Elastomers with Antioxidant and Retinoid-like Properties. ACS Biomater. Sci. Eng. 2, 268–277 (2016). [PubMed: 27347559]

47. Wang X et al. Influence of cell size on cellular uptake of gold nanoparticles. Biomater. Sci. 4, 970–978 (2016). [PubMed: 27095054]

48. Ngo JT et al. Click-EM for imaging metabolically tagged nonprotein biomolecules. Nat. Chem. Biol. 12, 459–465 (2016). [PubMed: 27110681]

49. Cherkezyan L et al. Nanoscale changes in chromatin organization represent the initial steps of tumorigenesis: a transmission electron microscopy study. BMC Cancer 14, 189 (2014). [PubMed: 24629088]

50. Dobin A et al. STAR: ultrafast universal RNA-seq aligner. Bioinform. 29, 15–21 (2013).

51. Wu T et al. ClusterProfiler 4.0: A universal enrichment tool for interpreting omics data. The Innovation 2, 100141 (2021). [PubMed: 34557778]

52. Love MI, Huber W & Anders S Moderated estimation of fold change and dispersion for RNA-seq data with DESeq2. Genome Biol. 15, 550 (2014). [PubMed: 25516281]

53. Zhou Y et al. Metascape provides a biologist-oriented resource for the analysis of systems-level datasets. Nat. Commun. 10, 1523 (2019). [PubMed: 30944313]

54. Li B & Dewey CN RSEM: accurate transcript quantification from RNA-Seq data with or without a reference genome. BMC Bioinform. 12, 323 (2011).

55. Bolger AM, Lohse M & Usadel B Trimmomatic: a flexible trimmer for Illumina sequence data. Bioinform. 30, 2114–2120 (2014).

56. Li H et al. The Sequence Alignment/Map format and SAMtools. Bioinform. 25, 2078–2079 (2009).

57. Lawrence M et al. Software for computing and annotating genomic ranges. PLOS Comput. Biol. 9, e1003118 (2013). [PubMed: 23950696]

58. Lee S, Cook D & Lawrence M Plyranges: A grammar of genomic data transformation. Genome Biol. 20, 4 (2019). [PubMed: 30609939]

59. Zhang Y et al. Model-based analysis of ChIP-Seq (MACS). Genome Biol. 9, R137 (2008). [PubMed: 18798982]

60. Yu G, Wang LG & He QY ChIPseeker: an R/Bioconductor package for ChIP peak annotation, comparison and visualization. Bioinform. 31, 2382–2383 (2015).

61. Dumanian ZP et al. Repair of critical sized cranial defects with BMP9-transduced calvarial cells delivered in a thermoresponsive scaffold. PLOS One 12, e0172327–e0172327 (2017). [PubMed: 28249039]

62. Goedhart J SuperPlotsOfData-a web app for the transparent display and quantitative comparison of continuous data from different conditions. Mol. Biol. Cell 32, 470–474 (2021). [PubMed: 33476183]
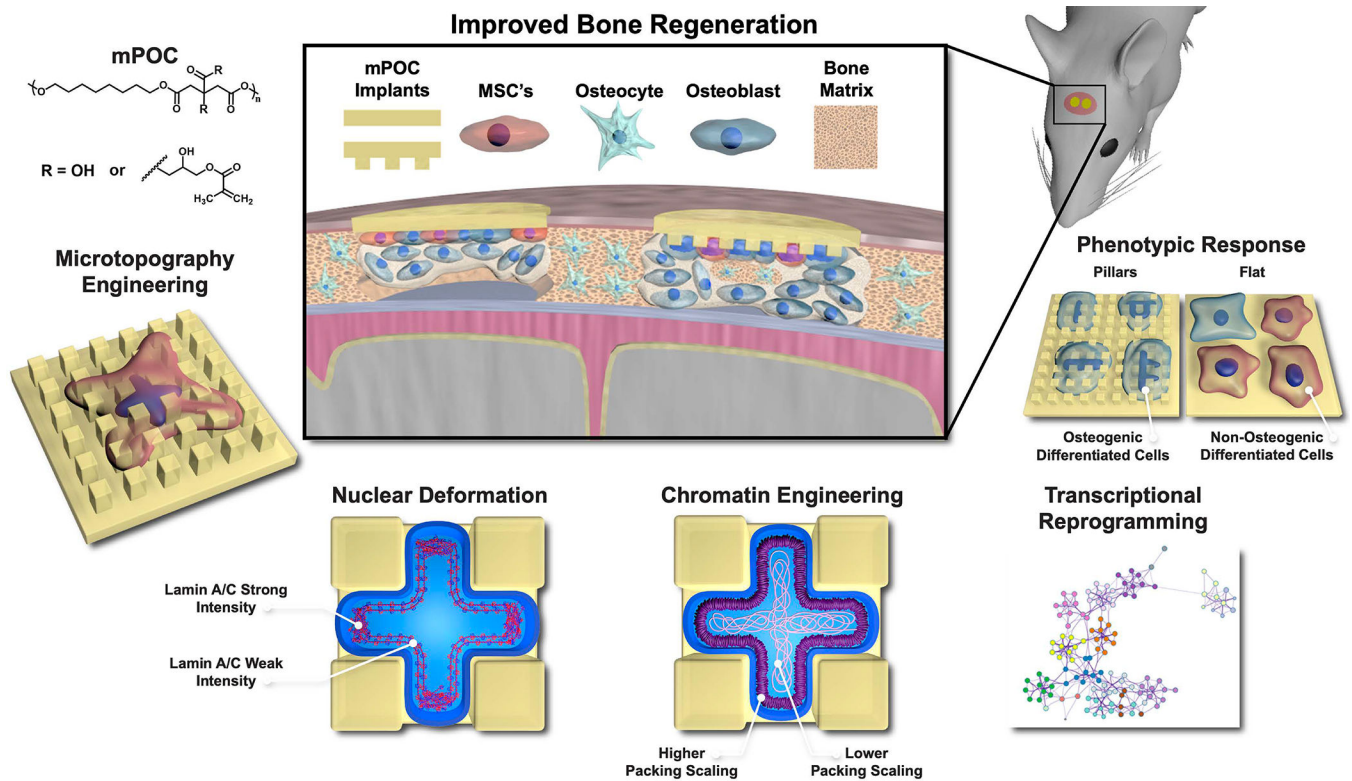
Figure 1. Schematic illustration of the influence of contact guidance-induced nuclear deformation on bone regeneration.

Microtopography engineering was utilized to create micropillar implants fabricated using mPOC, a citrate-based biomaterial. mPOC micropillars deformed hMSC nuclei and impacted overall nuclear morphology (nuclear volume and surface area), as well as lamin A/C organization at the nuclear periphery. As per modeling and experimental findings, nuclear deformation resulted in altered chromatin conformation, evaluated using average chromatin packing scaling, D. The decrease in average nuclear D was associated with an increase in response to directed differentiation towards the osteogenic lineage. Based on phenotypic assays for bone formation, contact guidance-induced nuclear deformation led to increased osteogenic differentiation of hMSCs *in vitro* and promoted bone regeneration *in vivo*.
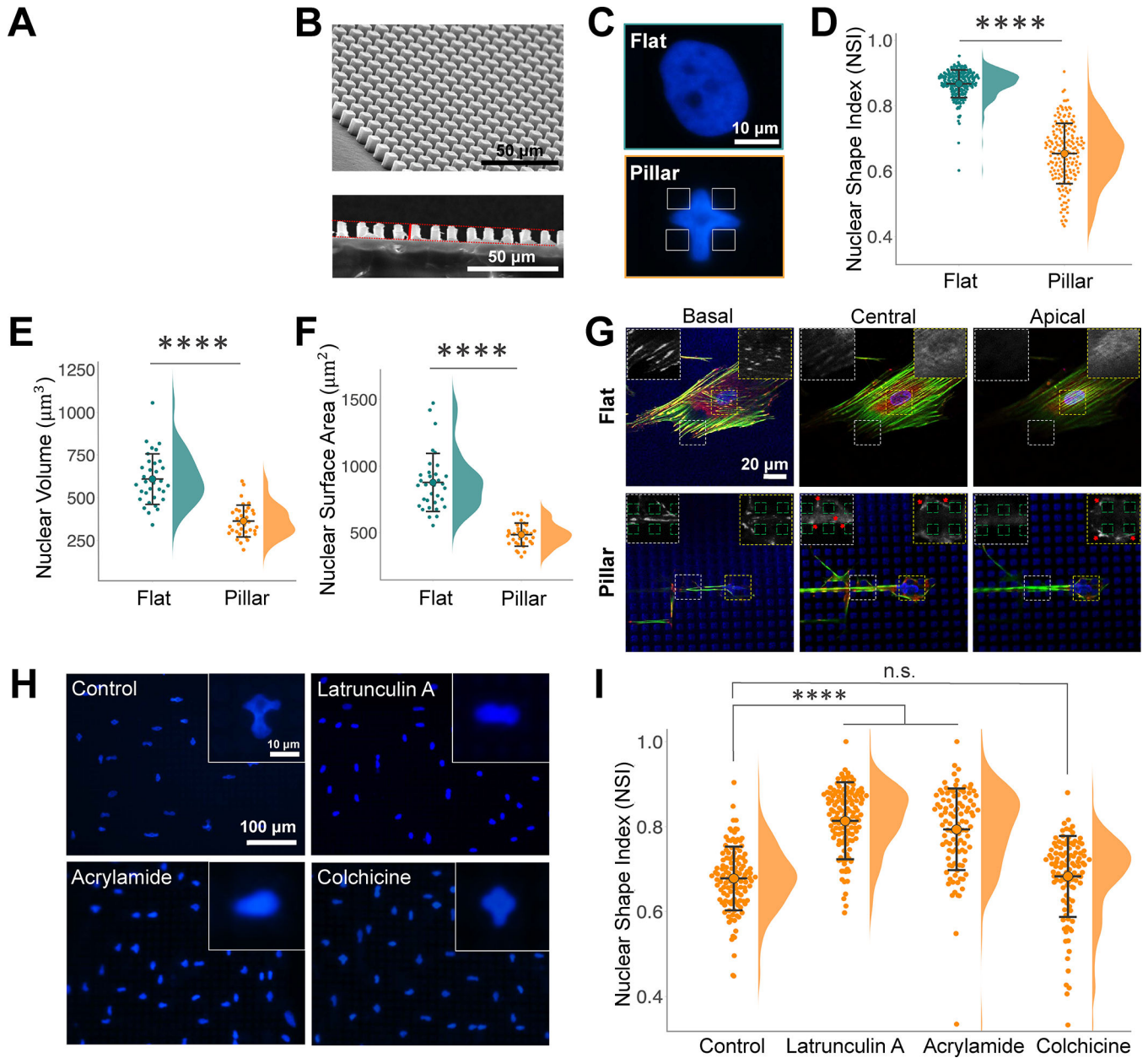
Figure 2. Micropillars modulate nuclear morphology by remodeling cytoskeleton components.
A. Phase-contrast image of square micropillars with the pillar size and spacing of 5×5 μm. **B**. SEM images showing the side (top) and section (bottom) view of the micropillars. **C.** DAPI staining images of hMSC nuclei on flat and micropillar substrates. **D.** Nuclear shape index (NSI) of hMSCs on flat (n=211 cells) and micropillar substrates (n=178 cells); N=4 independent experiments. **E.** Volume and **F.** surface area of hMSC nuclei on flat (n=33 cells) and micropillar (n=34 cells) surfaces; N=3 independent experiments. **G.** Cytoskeleton assembly of hMSCs on flat and micropillar surfaces shown using F-actin, vinculin, and DAPI staining images of hMSCs on flat and micropillar substrates at basal, central, and apical planes. Red arrows indicate FAs at central and apical planes. **H.** DAPI staining images of hMSC nuclei on micropillar surfaces with different pharmacological treatments to

disrupt the cytoskeleton assembly. **I.** NSI of hMSCs on micropillar surfaces with different cytoskeleton-disrupting treatments (n=121, 127, 101, 106 cells with treatment of control, Latrunculin A, Acrylamide, and Colchicine) after 6 hours of treatment; N=3 independent experiments (****p<0.0001, n.s., no significant difference). Data are presented as the mean and the standard deviation for each condition. Values from two groups were compared using Student's *t*-test (two-sided). For multiple groups, one-way analysis of variance (ANOVA) with Tukey's post-hoc test was used.
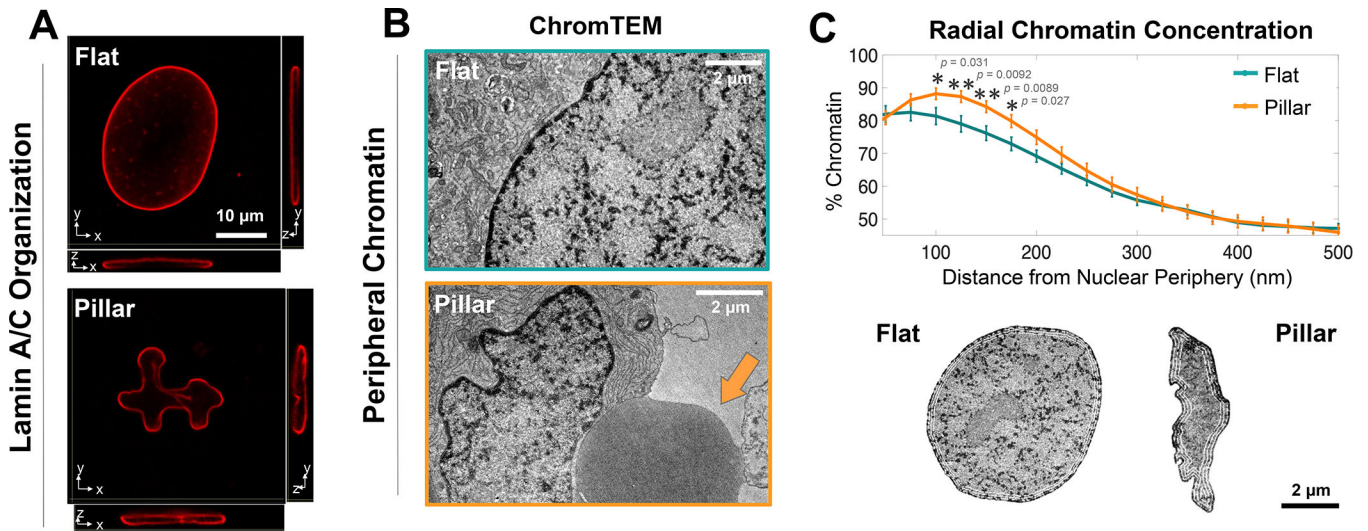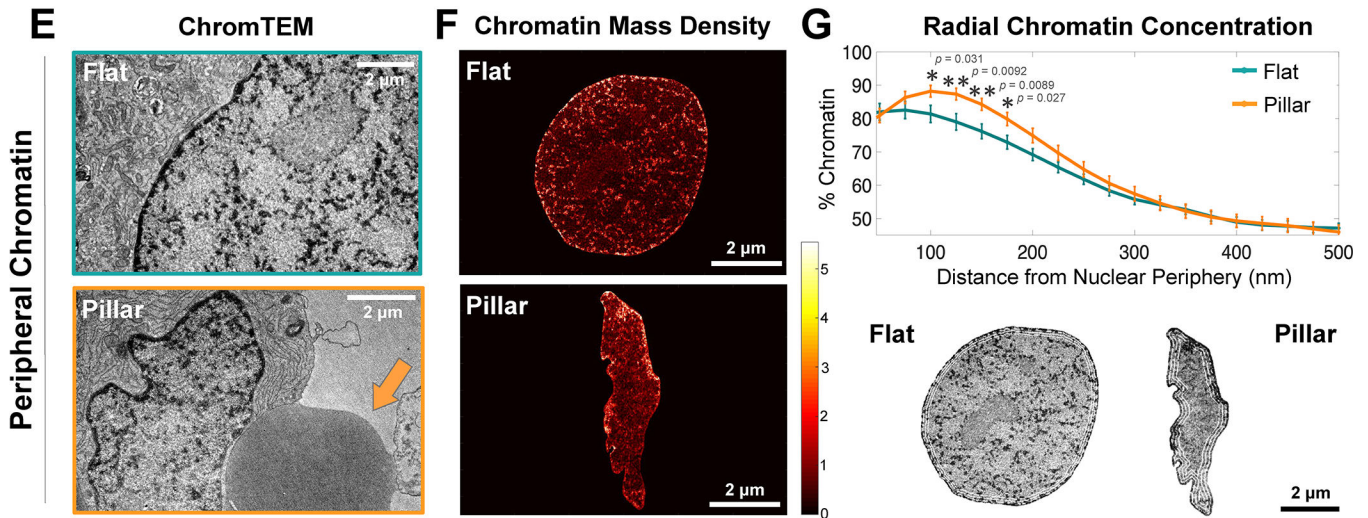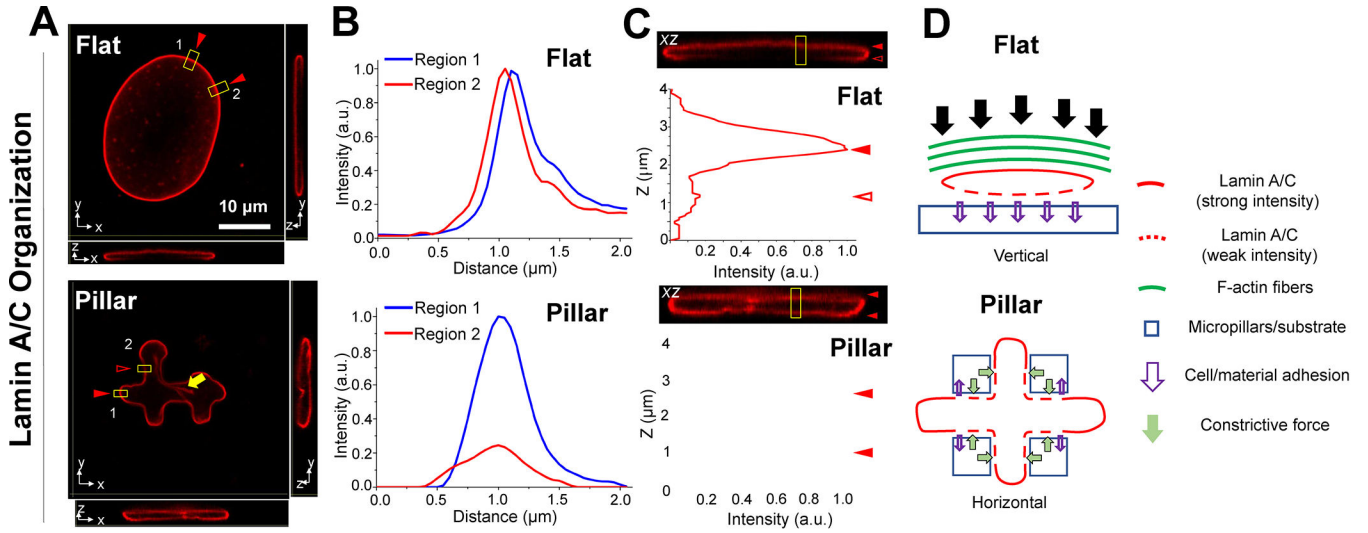
Figure 3. Micropillar-induced nuclear deformation is associated with alterations in nuclear structural components.

A. Lamin A/C staining images of hMSC nuclei on flat and micropillar surfaces. Solid red arrows indicate strong staining of lamin A/C; hollow red arrows indicate weak staining of lamin A/C; yellow arrows indicate wrinkles of lamin A/C surrounding micropillars. **B.** and **C.** show fluorescence intensity plot of lamin A/C along selected regions (yellow rectangles 1 and 2 in A) in the xy and (yellow rectangles in C) in the xz plane on flat and micropillar surfaces, respectively. **D**. Schematic summary of the influence of micropillars on the polarization of nuclear lamin A/C localization. On flat surfaces, actin-caps that formed above the nucleus compress it, and the cell adheres to the substrate beneath which leads to the burial of the epitope in polymerized lamin A/C at basal NE. On micropillars, the pillar structures prevented the expansion of the nucleus and led to its compression, and provided adhesion with cells that induced multimerization of lamin A/C around micropillars and induced horizontal polarization of NE. **E.** ChromTEM images of 50 nm thick resin sections of hMSCs seeded on flat and micropillar surfaces. The technique resolves nucleoli, nuclear speckles, and mitochondria at high resolution. The orange arrow shows the location of micropillars. **F.** Colormap of Chromatin Mass Density of Nucleus obtained from ChromTEM images on flat and micropillar surfaces (generated using hot colormap on MATLAB). Scale bar demonstrating low (black) to high (white) chromatin mass density (a.u.) **G.** Top: Radial Chromatin concentration analysis defined by the percentage of chromatin within consecutive 25 nm thick bands as a function of the distance from its location to the nuclear periphery. The result was calculated for segmented hMSC nuclei from ChromTEM images on flat (n=10 cells) and micropillar surfaces (n=16 cells), indicating a drastic change in the peripheral chromatin organization. Data are presented as the mean and the standard error and statistics were compared using Student's *t*-test (two-sided). N=2 independent experiments. Bottom: ChromTEM images show radial bands at 25 nm, 250 nm, 500 nm, and 750 nm.
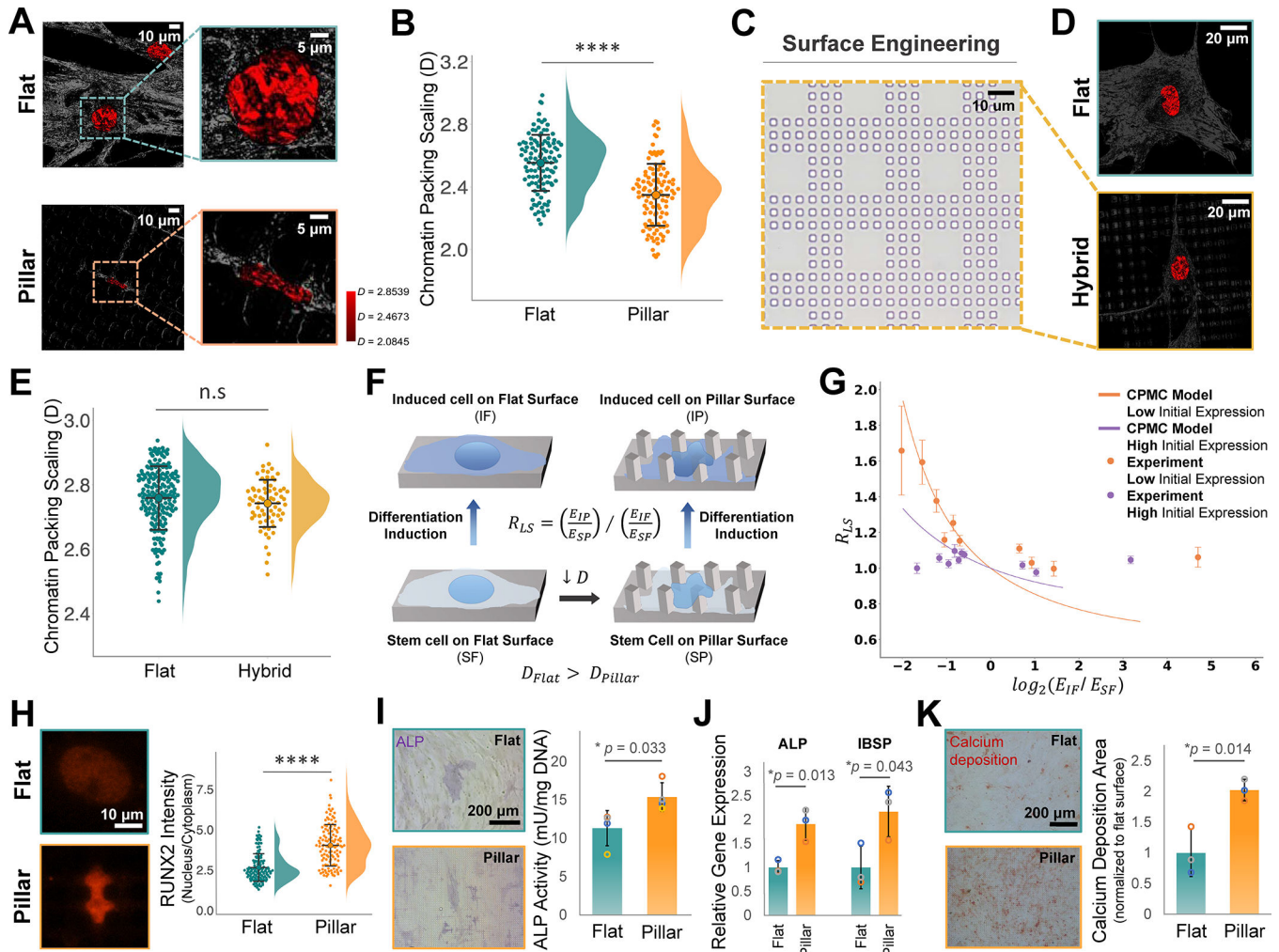
Figure 4. A decrease in chromatin packing scaling in deformed nuclei enhances the responsiveness of hMSCs to osteogenic differentiation.

A. PWS microscopy of hMSCs shows a significant change in average chromatin packing scaling, *D* in deformed nuclei compared to control. Stem cells on flat and micropillar surfaces show changes in packing domains (red clusters). **B.** Micropillars deform cell nuclei and significantly decrease average *D* in stem cells on micropillar surfaces (n=110 hMSCs) when compared to cells cultured on flat surfaces (n=111 hMSCs); N=4 independent experiments. **C.** Hybrid micropillar patterns with a 35×35 μm flat region surrounded by 5×5 μm pillars were designed to prevent nuclear deformation. **D.** PWS microscopy of hMSCs shows no significant change in average *D* on hybrid micropillar patterns compared to control. **E.** hMSCs cultured on hybrid micropillar patterns (n=70 cells) show no significant change in average *D* relative to cells cultured on flat surfaces (n=196 cells); N=3 independent experiments. **F.** hMSCs seeded on a flat surface (high *D*) and micropillar surface (low *D*) (SF and SP, respectively) were induced to differentiate towards osteogenic lineage (IF and IP, respectively). E denotes expression rate in the respective conditions used to evaluate lineage-specific responsiveness coefficient, R_{LS}, a measure of response to differentiation induction (osteogenic differentiation in this case) on the micropillar

surface compared to the flat surface. **G**. Lineage-specific transcriptional response due to differentiation induction increases in low D cells. The analysis was performed for a total of 1513 differentially expressed genes with p-adjusted<0.05 and |fold change|>1.5 for initially lowly expressed genes (orange) and initially highly expressed genes (purple) in the control hMSCs (SF). Data are presented as the mean and the standard error of each quantile for initially underexpressed genes (in orange) and initially overexpressed genes (in purple). **H.** Left: RUNX2 staining images. Right: Nuclear to cytoplasmic RUNX2 in hMSCs on flat (n=123 cells) and micropillars (n=119 cells), N=3 independent experiments. **I.** Left: ALP staining images. Right: ALP activity analysis of hMSCs after 7-day osteogenic differentiation induction; n=4 samples. **J.** Relative gene expression of ALP and IBSP tested after osteogenic induction for 7 days of hMSCs on flat and micropillar surfaces, n=3 samples. **K.** Left: Calcium deposition after osteogenic differentiation for 3 weeks on flat and micropillar surfaces as per Alizarin Red S (ARS) staining. Right: Positive ARS-stained area normalized to a flat surface. n=3 samples. (****p<0.0001, n.s. = not significant). All data are presented as the mean and the standard deviation except in **G**. Statistics were compared using Student's t-test (two-sided).
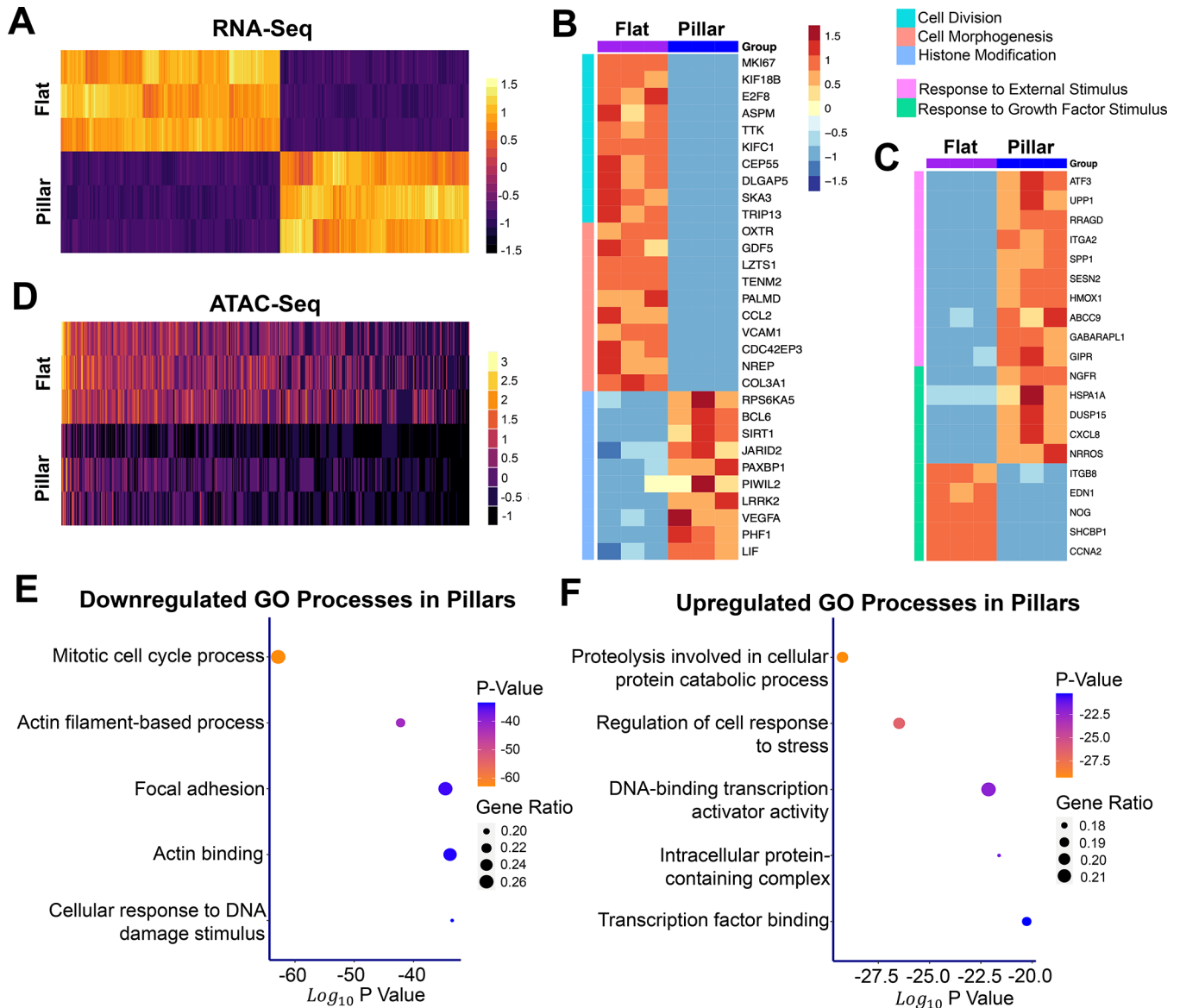
Figure 5. Chromatin accessibility and gene expression alter the hMSC phenotype when cultured on micropillars.

A. Top 1000 differentially expressed genes identified using RNA-Seq performed on hMSCs cultures on flat and micropillar surfaces. RNA-Seq heatmap of differentially expressed genes associated with selected phenotypic processes in **B.** stem and **C.** osteogenic induction medium in hMSCs cultured on micropillars compared to flat surfaces. **D.** Top 1000 differentially open-genic features identified using ATAC-Seq performed on hMSCs cultures on flat and micropillar surfaces. **E.** Integration of ATAC-Seq and RNA-Seq to determine top **E.** downregulated and **F.** upregulated gene ontology processes in hMSCs cultured on micropillars. 6411 differentially expressed genes identified using the intersection of RNA-Seq by ATAC-Seq were used to determine the processes using Metascape. Metascape utilizes hypergeometric test and Benjamini-Hochberg p-value correction algorithm to determine enriched GO terms.
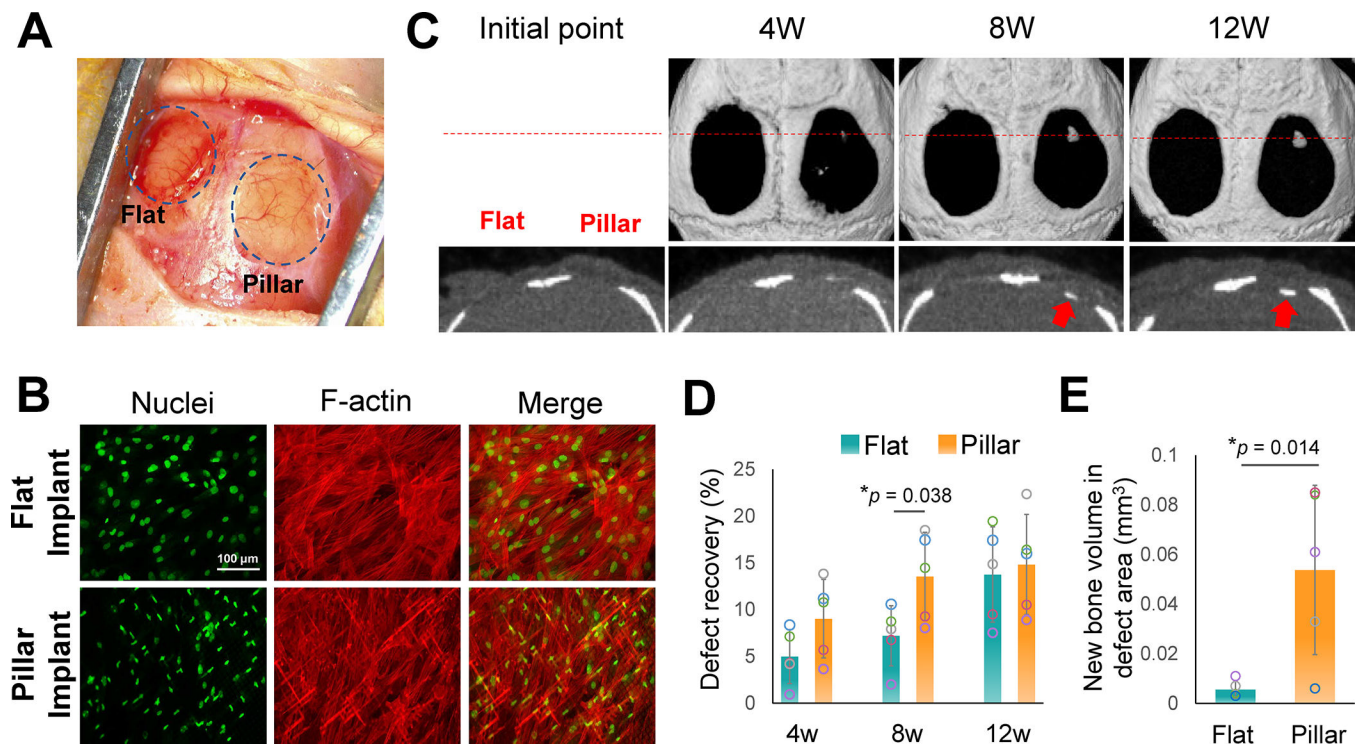
Figure 6. Micropillar-induced nuclear deformation promotes bone regeneration *in vivo*.
A. Two critical-sized cranial defects with a diameter of 4 mm were created, followed by implantation of hMSC-seeded flat and micropillar mPOC scaffolds. **B**. Staining of nuclei (green) and F-actin (red) of hMSCs seeded on free-standing flat and micropillar mPOC scaffolds. **C**. Representative µCT images of a typical animal implanted with hMSC-seeded flat (left) and micropillar (right) scaffolds were acquired serially at weeks 0, 4, 8, and 12 post-surgery. Red arrows indicate newly formed bone. **D**. Calvarial defect recovery percentage after 4, 8, and 12 weeks of surgery with flat and micropillar implants (n=5 animals). **E**. Newly formed bone volume in the defect region treated with flat and micropillar implants (n=5 animals). Data are presented as the mean and the standard deviation. Statistics were compared using Student's *t*-test (two-sided).
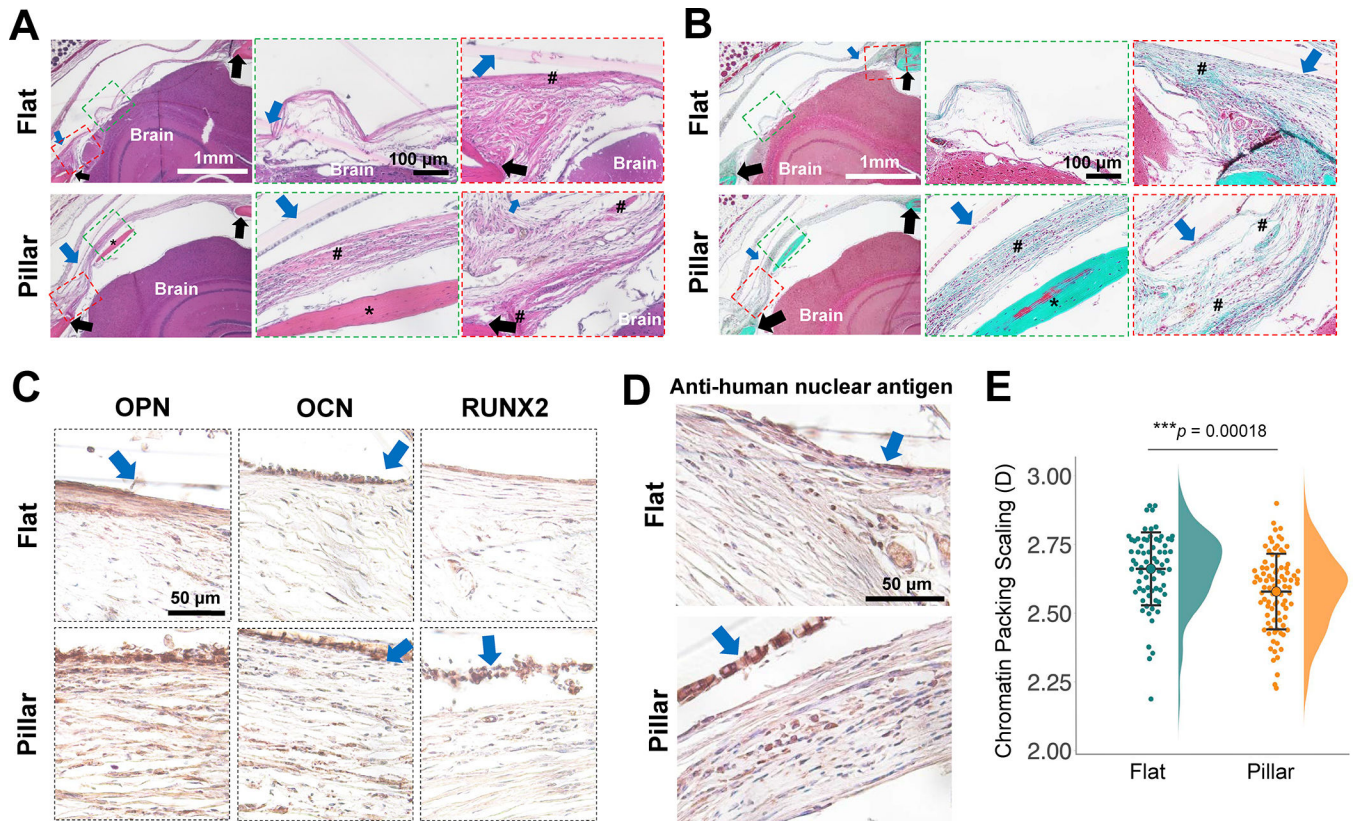
Figure 7. Micropillars facilitate osteogenesis via chromatin reprogramming *in vivo*.
A. H&E and **B**. trichrome staining of calvarial defect tissue treated with flat and micropillar implants. Black arrows indicate bone defect edge; blue arrows indicate implants; # indicates osteoid tissue formation, and * indicates mature bone formation according to histology staining images. **C**. IHC staining of OPN, OCN, and RUNX2 of regenerated tissue in bone defects with flat and micropillar implants. **D**. IHC staining of anti-human nuclear antigen in regenerated tissue treated with flat and micropillar implants. **E**. PWS microscopy shows a significant decrease in average chromatin packing scaling, *D* in deformed nuclei on micropillar (n=89 cells) implants when compared to nuclei on flat (n=71 cells) implants (N=5 rodents, ****p<0.0001). Data are presented as the mean and the standard deviation. Statistics were compared using Student's *t*-test (two-sided).